Check for updates

EcoEnergy

WILEY

EcoEnergy Open Access

PERSPECTIVE OPEN ACCESS

Challenges and Opportunities in the Use of Iron Photosensitizers for Dye-Sensitized Solar Cells and Photoelectrosynthetic Cells Applications

Lakshmi Narayan Satheesh[1] | Katerina Achilleos[1] | Abdullah M. Abudayyeh[1] | Ludovic Troian-Gautier[1,2]

[1]Molecular Chemistry, Materials and Catalysis (MOST), Institute of Condensed Matter and Nanosciences (IMCN), UCLouvain, Louvain-la-Neuve, Belgium | [2]Wel Research Institute, Wavre, Belgium

Correspondence: Ludovic Troian-Gautier (Ludovic.Troian@uclouvain.be)

Received: 19 August 2024 | **Revised:** 5 February 2025 | **Accepted:** 16 February 2025

Funding: This work was supported by Fonds De La Recherche Scientifique—FNRS. This publication benefited from the support of the Walloon Region as part of the financing of the FRFS-WEL-T strategic axis.

Keywords: DSPEC | DSSC | iron | photosensitizers | solar fuels

ABSTRACT

Novel renewable alternatives to meet the needs of our current energy landscape are highly sought after. Photovoltaic solar cells (PV) are considered leading candidates for carbon neutrality due to their numerous benefits and good solar-to-energy conversion efficiency. However, the need is no longer solely focused on electric current generation but also on strategies to store that energy. This led, amongst other technologies, to the development of dye-sensitized photoelectrosynthesis cells (DSPECs), the successor of dye-sensitized solar cells (DSSCs). However, these cost-effective solar cells mostly use photosensitizers based on scarce metals such as ruthenium. Iron-based photosensitizers represent the holy grail due to their low toxicity, greater abundance, and versatile chemistry. However, they still suffer from drastic limitations: their photochemistry and extremely fast excited-state deactivation processes lead to inefficient charge injection and/or fast charge recombination. This review gathers examples of iron-based photosensitizers that have been successfully immobilized on metal oxide surfaces. A critical comparison of Fe-based photosensitizers is made based on their photophysical properties, electrochemistry, and photovoltaic performances.

1 | Introduction

The current large-scale use of fossil fuels, coal, crude oil, and natural gas has resulted in a tremendous amount of carbon dioxide and other greenhouse gases being released into the atmosphere. This has led to several problems, such as, but not limited to, climate change and ocean acidification, that have exerted an enormous burden on the globe [1]. The 2015 Paris Climate Change Agreement, signed by 195 countries, emphasized the need for serious actions to remediate climate change and limit the average global temperature rise to below 2°C compared to pre-industrial levels [2]. Furthermore, the European Union has set the ambitious goal to become climate-neutral by 2050 and thus become an economy with net-zero greenhouse gas emissions. This objective represents the core of the "European Green Deal." Many other countries have also answered nature's call and realized the urgent necessity to develop carbon neutral, or carbon zero fuels, with production driven by widely available, accessible, and renewable sources of energy, such as wind, geothermal, biomass, and solar [3]. Solar energy is highly attractive because of the wide range of wavelengths that reach the Earth and its abundance and broad accessibility [4]. It is estimated that the sun provides enough energy in 1 h (4.3×10^{20} J) to cover our yearly energy consumption [5]. The idea of using sunlight as a clean

Lakshmi Narayan Satheesh, Katerina Achilleos, and Abdullah M. Abudayyeh contributed equally to this study.

This is an open access article under the terms of the Creative Commons Attribution License, which permits use, distribution and reproduction in any medium, provided the original work is properly cited.

© 2025 The Author(s). *EcoEnergy* published by John Wiley & Sons Australia, Ltd on behalf of China Chemical Safety Association.

energy source is not novel; it was already proposed by Giacomo Ciamician in 1912 in his famous essay: "The Photochemistry of the Future" [6]. However, we still have some ways to go before his vision of solar energy harvesting becomes a reality.

One of the most important developments in the 20th century most probably originated in Bell's laboratory, which developed the first photovoltaic solar cell (PV) in 1956 [7]. This discovery revolutionized the energy landscape, and nowadays, with the ease of production, decreased costs, and optimized manufacturing process, PVs are a prominent candidate for climate neutrality. Current PVs, used to convert solar energy to electricity, have an efficiency of ~25% in sunlight harvesting [8, 9], with a record-breaking 33.9% reached this year for tandem silicon-perovskite solar cells [10]. A significant challenge of using sunlight is its intermittent nature and the diurnal cycle; therefore, it becomes essential to "store" solar energy [11]. One great alternative is to store the electricity produced by PVs in batteries [12–14]. However, low energy densities (0.3–0.9 MJ/kg, 0.9–2.4 MJ/L) suggest that battery energy densities are approaching a ceiling even when using some of the lightest elements in the periodic table. In addition, the environmental costs associated with mining lithium, for example, are concerning and will become unsustainable for the large-scale implementation of batteries in our daily lives (energy storage, electric vehicles, etc.). An alternative is to store this energy in the smallest volume in which electrons can be stored: a chemical bond [15, 16]. Indeed, liquid fuels such as gasoline have much greater energy densities of ~50 MJ/kg (~35 MJ/L) than any battery, and hydrogen gas has an even greater energy density of 140 MJ/kg (9.17 MJ/L at 700 bar). PVs can be used to power water electrolyzers used in green hydrogen production. However, such electrolyzers still suffer from high overpotentials and the high initial cost of the electrodes, membranes, and other electrolyzer components. The price of hydrogen produced by water electrolyzers is still much higher than hydrogen produced through conventional methods. However, there is no doubt that large-scale electrolyzers that generate hydrogen solely powered by renewable energy will become more efficient and affordable. Energy diversification will be key to overcoming many of the world's challenges in the coming years. As such, developing photoelectrosynthesis cells is an important alternative. In photoelectrosynthesis cells, solar energy drives desirable chemical transformations such as water splitting, hydrogen production, halide oxidation, or CO_2 reduction [17–19]. Mimicking plants and storing light energy in chemical bonds, forming so-called "solar fuels," is highly attractive, mainly when producing high-energy density carbon-zero fuels such as hydrogen [9, 16, 20, 21]. Since the pioneering works of Fujishima and Honda [4, 22] using TiO_2 photoelectrodes for the photoelectrochemical water splitting, tremendous efforts to develop artificial photochemical systems for solar fuels generation have been made [23–25].

2 | Dye-Sensitized Photoelectrodes

2.1 | Dye-Sensitized Solar Cells (DSSC)

A limitation of the pioneering work of Fujishima and Honda was the need for a direct band gap excitation of TiO_2, which occurs in the UV region of the solar spectrum. This part of the solar spectrum is highly energetic but, unfortunately, not very abundant at the surface of the Earth, which limits the overall efficiency of such devices. However, this did not limit their widespread use in large-scale solar conversion applications by pioneers such as Kazunari Domen [7, 26, 27], amongst others [28]. Water-splitting devices with quantum yield efficiencies almost reaching unity have been recently reported [26]. In these devices, the overall water splitting is driven by 350–360 nm irradiation using an aluminum-doped $SrTiO_3$ photocatalyst [29, 30]. The hydrogen and oxygen evolution reactions were promoted by selective photodeposition of Rh/Cr_2O_3 [31] and CoOOH [32] co-catalysts on different facets of the semiconductor crystal.

To absorb visible light, new materials must be developed, or existing ones, such as SnO_2 or TiO_2, must be sensitized to visible light through the use of organic or inorganic photosensitizers. In the 60s and 70s, Gerischer developed a model to define the principles of heterogeneous electron transfer on the semiconductor/electrolyte interface [33, 34]. Although the first photovoltaic device was produced in 1954 by Bell Laboratories, intense research on solar cells did not emerge until the OPEC energy crisis of 1973 [35]. Seminal work by H. Gerischer, J. B. Goodenough, and A. Kirsch-De Mesmaeker on dye-sensitized single crystal photoelectrodes, accompanied by groundbreaking work by H. Taube, R. Marcus, N. Hush, W. F. Libby, and N. Sutin on electron transfer, enabled the development of DSSC by M. Grätzel and B. O'Regan in 1991 (vide infra) [36–46]. Liquid junction cells with a solar conversion efficiency of around 11% evolved in the 1970s–1980s owing to the realization of pure single-crystal materials [47]. In the mid-1970s, Heller proposed employing inexpensive polycrystalline semiconductors for photoelectrosynthesis cells instead of highly pure electronic-grade semiconductors [48, 49]. Consequently, in 1976, Hodes and coworkers conducted pioneering work using polycrystalline chalcogenide electrodes for electrochemical energy conversion [50]. Alonso et al. [51] and Matsumura, Nomura, and Tsubomura [52] sensitized ZnO electrodes with Rhodamine B, rose Bengal, and other related dyes to enhance efficiency. Still, the conversion yields from light to electricity remained well below 1%.

A breakthrough in the field occurred in 1991 when Grätzel and O'Reagan used mesoporous TiO_2 instead of a single crystal, sensitized with a ruthenium-based photosensitizer combined with an iodide/triiodide redox mediator. The attachment of photosensitizers to TiO_2 can be successfully achieved using various anchoring groups such as carboxylic acid ($-CO_2H$) and phosphonic acid ($-PO_3H_2$) groups [53], the latter being stable on a broader pH range. Other robust anchoring groups that have thus far been less explored include hydroxamic acids, silatranes, siloxanes, and diazoniums [54–56]. The so-called dye-sensitized solar cells that harvest a high proportion (46%) of the incident solar flux have an overall light-to-electric energy conversion efficiency of up to 7.9% and 12% in simulated solar light and diffuse daylight, respectively [36]. Dye-sensitized solar cells have been reviewed in many instances, so the reader is directed toward these excellent reviews [11, 36, 57, 58]. It is however essential to describe the main components and operating principles of DSSCs to understand the underlying processes.

28359399, 0, Downloaded from https://onlinelibrary.wiley.com/doi/10.1002/ece2.70001, Wiley Online Library on [09/03/2025]. See the Terms and Conditions (https://onlinelibrary.wiley.com/terms-and-conditions) on Wiley Online Library for rules of use; OA articles are governed by the applicable Creative Commons License

The primary components of DSSCs are the photoanode, the counter electrode, the photosensitizer, and the electrolyte (Figure 1). The electrodes are made of transparent, conductive glass such as indium or fluorine-doped tin oxide (ITO or FTO) [59]. The electrode is coated with an inexpensive semiconductor material, commonly mesoporous anatase TiO_2, but other materials have also been used, such as WO_3, ZnO, and SnO_2 [60, 61]. The counter electrode can consist of carbon, graphite, or some conductive polymers. The counter electrode acts as an electron collector and is therefore necessary to complete the circuit and ensure rapid electron exchange. Platinum remains the most efficient material commonly used as a counter electrode in standard DSSCs [62]. The electrons delivered by the counter electrode are used to reduce the redox mediator in the electrolyte, filling the gap between the two electrodes. Iodide/triiodide (I^-/I_3^-) is the most widely used redox mediator in standard DSSCs, with cobalt polypyridine derivatives coming a close second [63]. Alternative redox mediators include the pseudohalogen $(SeCN)_2/SeCN^-$, which has scored a 20% incident photon to current efficiency [64], or disulfide/thiolate, which reached an efficiency of 6.25% [65]. Mechanistically, upon sunlight irradiation, the photosensitizer absorbs photons that have enough energy to promote a ground-to-excited-state transition (Figure 1). This excited photosensitizer should have enough energy to transfer an electron into the conduction band (or acceptor states) of mesoporous TiO_2 so that the electron injection process from the excited photosensitizer to TiO_2 occurs efficiently [66–68]. The photosensitizer is then regenerated by I^-, generating the corresponding iodine atom ($I^\bullet$), that can then form $I_2^{\bullet-}$ upon reaction with iodide. Note that a concerted pathway, that would save approximately 300 mV, has been proposed, where regeneration of the photosensitizer and $I_2^{\bullet-}$ formation occur in one concerted step [69]. The previously mentioned photo-injected electron travels through the external circuit to reach the platinum-coated FTO counter electrode, which is used to reduce triiodide (I_3^-) [62]. The resulting open-circuit photovoltage of this cell depends on the difference between the solid electrode's Fermi level and the electrolyte's redox potential.

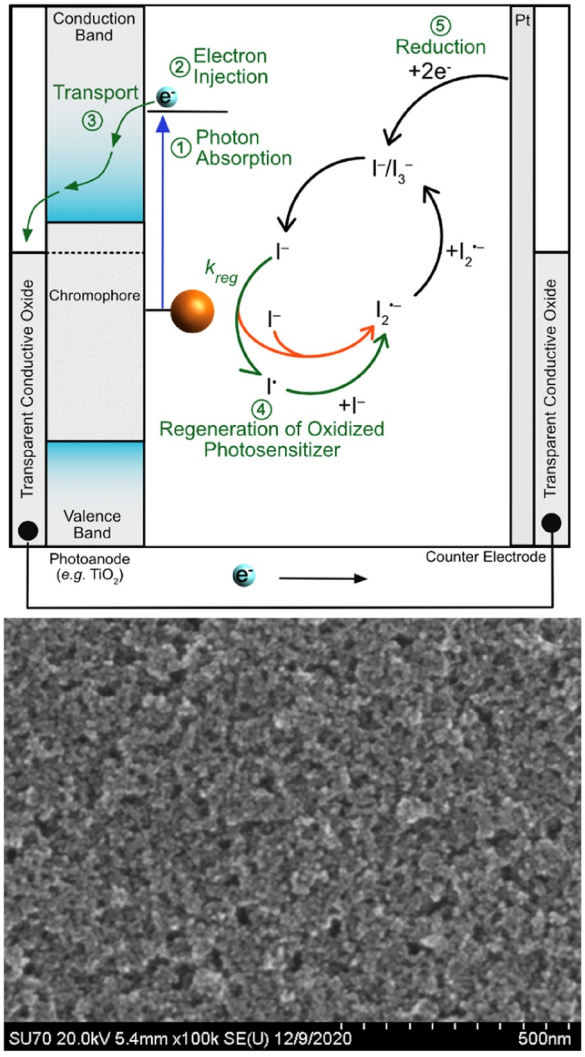


FIGURE 1 | (Top) Schematic representation of a DSSC: The photosensitizer (orange sphere), once excited by visible light, injects one electron into TiO_2 and is after that regenerated via the transfer of one electron from iodide that finally forms $I_2^{\bullet-}$ either in consecutive steps (green arrows) or according to a concerted mechanism (orange arrow). The electron injected into TiO_2 is shuttled to the counter electrode where it can reduce triiodide (I_3^-). (Bottom) SEM image of mesoporous TiO_2 (17 ± 3 nm particle size) used as metal oxide for the construction of photoanodes.

2.2 | Dye-Sensitized Photoelectrosynthesis Cells (DSPEC)

In DSSCs, the redox mediator and arrangement of the different components ensure that sunlight is converted into electricity and that no net chemical reactions occur. Going further, the main idea with DSPECs was to eliminate the need for a redox mediator by performing a permanent chemical transformation and to use the injected electrons to drive reductive catalysis at the counter electrode. The photoanode is similar to the one used in DSSCs and, as such, is mainly composed of TiO_2 or SnO_2/TiO_2 core–shell structures [70–74]. The photosensitizer is excited with visible light and injects electrons into the semiconductor's conduction band or acceptor states. This results in the instantaneous localization of a hole on the oxidized photosensitizer. In DSPECs, the photosensitizer is regenerated by transferring the hole to a water oxidation catalyst that, upon further hole transfers, oxidizes water into O_2 and H^+ (Figure 2, left). Alternatively, the hole can be transferred to halides in solution and thus perform halide oxidation. However, this requires a careful balance between ground and excited-state reduction potentials to enable both excited-state electron injection and hole transfer [75–77]. Exploiting the hole generated in the DSPEC half cells for biomass conversion is also of great interest [78]. For example, the selective oxidation of the C–O bond as a model for that found in lignin conversion technology has recently been achieved using dye-sensitized TiO_2 photoanodes [79].

The photocathode is typically composed of a p-type semiconductor such as NiO or $Cu(In,Ga)Se_2$ [7]. Upon light absorption, the excited photosensitizer injects a hole into the semiconductor's valence band while the electron is transferred to the catalyst, which performs reductive catalysis, such as H^+ or CO_2 reduction (Figure 2, right).

28359399, 0, Downloaded from https://onlinelibrary.wiley.com/doi/10.1002/ece2.70001, Wiley Online Library on [09/03/2025]. See the Terms and Conditions (https://onlinelibrary.wiley.com/terms-and-conditions) on Wiley Online Library for rules of use; OA articles are governed by the applicable Creative Commons License

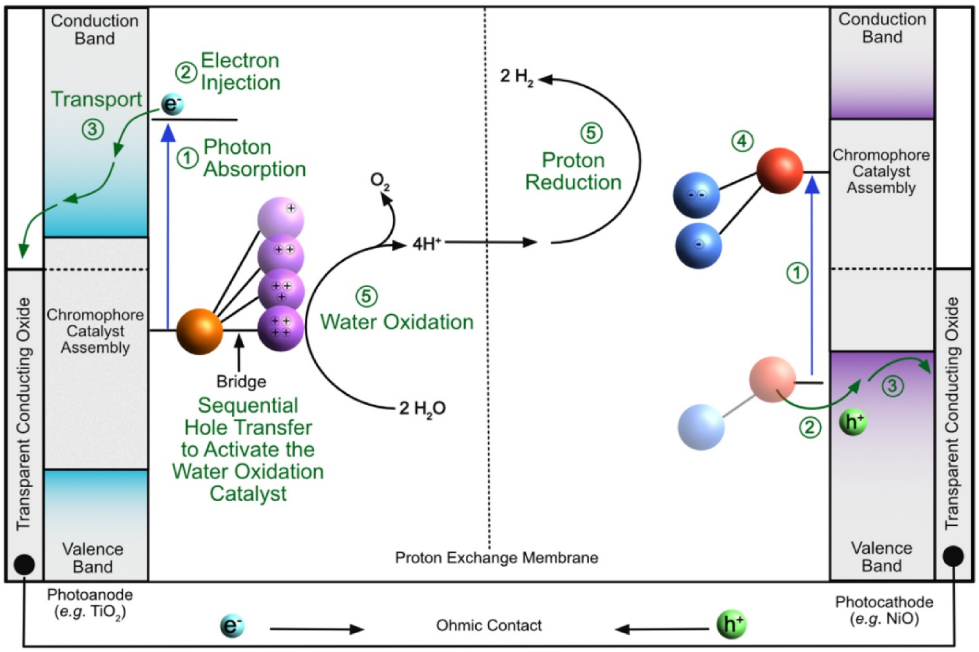


FIGURE 2 | DSPEC device where water oxidation occurs on the photoanode and proton reduction on the photocathode: The photosensitizer (orange sphere), once excited by visible light, injects one electron into TiO_2 and is after that regenerated via the transfer of one electron from a precatalytic species (hole transfer and purple spheres). Through several transfers, the precatalytic species is converted into an active catalyst for water oxidation. The electrons injected into TiO_2 are shuttled to the photocathode where light activation of the photosensitizer (red sphere) leads to a sequence of hole/electron transfer to activate a proton reduction catalyst (blue sphere).

In 1999, T. J. Meyer designed the first dye-sensitized photoelectrosynthesis cells [80]. This was a significant scientific breakthrough where, on the one hand, interfacial electron transfer was used to generate a photocurrent (< 10 $\mu A/cm^2$) and, on the other hand, the oxidized photosensitizer was regenerated by a catalyst that could, in turn, perform a chemical transformation, for example, the oxidation of isopropanol to acetone. A decade later, T. E. Mallouk and coworkers reported a water-splitting DSPEC [81] that combined a heteroleptic Ru(II) tris(bipyridine) photosensitizer immobilized on a TiO_2 thin film through phosphonate anchoring groups and an IrO_x water oxidation catalyst [82]. The reaction mechanism was investigated through solution-phase studies using 1M $Na_2S_2O_8$ as a sacrificial electron acceptor and showed that efficient oxidative excited-state electron transfer occurred from the ruthenium photosensitizer, generating the oxidized Ru(III) photosensitizer and the reduced electron acceptor. Regeneration of the ground-state photosensitizer was driven by the IrO_x water oxidation catalyst with a 2-ms time constant. On TiO_2, the open-circuit photovoltage profile obtained in pH 5.75 buffered solution in the presence of Na_2SiF_6 and Na_2SO_4 yielded an open-circuit potential of about −325 mV versus Ag/AgCl combined with a steady photocurrent of 10–30 $\mu A\ cm^{-2}$ and a ~20% photoanodic water to oxygen generation efficiency, thus showing great promise for these kinds of applications using visible light.

In 2012, Sun and coworkers reported one of the first examples of a dye-sensitized photocathode for proton reduction using a visible-light-driven photoelectrosynthesis cell [83]. This pioneering work used an organic dye as the PS, a cobaloxime complex as the hydrogen evolution catalyst, and nano-NiO as the photocathode. When a potential of −0.4 V versus Ag/AgCl was applied, this system generated a photocurrent density of around 20 $\mu A\ cm^{-2}$ with a concentration of hydrogen that reached a value of ca. 322 nmol in 6 min after which leaching of the catalyst occurred. This amount of hydrogen accounted for 2 turnovers based on the catalyst and 6 based on the PS.

Additionally, extensive effort has been devoted to DSPECs mimicking photosystem II (PSII) [84, 85]. For example, T. J. Meyer and coworkers recently reported an electrode using a carbazole mediator that enabled water oxidation using efficient interfacial hole transfer from the Fe_2O_3 light absorber to a Ru catalyst [86]. More recently, G. J. Meyer and coworkers showed that mesoporous films comprising SnO_2 core and TiO_2 shell (SnO_2/TiO_2) have potential practical applications in DSPECs for water splitting due to their superior performance compared to conventional sensitized TiO_2 or SnO_2 electrodes [87]. In these architectures, the excited photosensitizer injects an electron in the TiO_2 shell that is then transferred to the SnO_2 core through a thermodynamic gradient. Back electron transfer from the electron in SnO_2 to the oxidized photosensitizer is then drastically slowed down [88]. In addition, the TiO_2 shell can shield an electric field from a surface-anchored dye by a factor of 4 [89].

2.3 | Metrics to Quantify the Efficiency of DSSC and DSPEC Devices for Solar Production

Several metrics are used to quantify the efficiency and performance of DSPEC devices. In here, the metrics have been organized in terms of electrical (Equations 1–5), spectral (Equations 6–8), and catalytic (Equations 9 and 10) efficiencies.

28359399, 0, Downloaded from https://onlinelibrary.wiley.com/doi/10.1002/ece2.70001, Wiley Online Library on [09/03/2025]. See the Terms and Conditions (https://onlinelibrary.wiley.com/terms-and-conditions) on Wiley Online Library for rules of use; OA articles are governed by the applicable Creative Commons License

Electrical efficiencies

$$\eta_{STH} = \frac{P_{output}}{P_{input}} = \frac{J_{sc}\left(\text{mA/cm}^2\right) \times (1.23\ \text{V}) \times \eta_F}{P_{light}\ (\text{mW/cm}^2)} \quad (1)$$

$$\eta_{SFE} = \left[\frac{J_{OP}\left(\text{mA/cm}^2\right) \times (V_{redox}) \times \eta_F}{P_{light}\ (\text{mW/cm}^2)}\right]_{AM\ 1.5G} \quad (2)$$

$$ABPE = \frac{P_{output}}{P_{input}} = \frac{J_{sc}\left(\text{mA/cm}^2\right) \times (V_{redox} - V_{app}) \times \eta_F}{P_{light}\ (\text{mW/cm}^2)} \quad (3)$$

$$\eta = \frac{V_{oc}\, J_{sc}\, FF}{P_{in}} \quad (4)$$

$$FF = \frac{P_{max}}{V_{oc}\, J_{sc}} \quad (5)$$

Spectral efficiencies

$$IPCE(\lambda) = \frac{\text{electron flux}}{\text{photon flux}} = \frac{hc}{e}\ \frac{J\left(\text{mA/cm}^2\right)}{\lambda \times P_\lambda} \quad (6)$$

$$IPCE(\lambda) = LHE(\lambda)\, \phi_{inj}\, \eta_c \quad (7)$$

$$\phi_{inj} = \frac{k_{inj}}{\sum_i^n k_i} \quad (8)$$

Catalytic efficiencies

$$TON = \frac{\text{moles of product}}{\text{moles of catalyst}} \quad (9)$$

$$TOF = \frac{\text{moles of product}}{\text{moles of catalyst x time}} \quad (10)$$

An important metric is the solar-to-hydrogen (or solar-to-fuel) conversion efficiency (STH). This correlates the energy input (solar irradiation) to the energy output, as shown in Equation (1) [90]. The energy output is determined by the amount of hydrogen produced under illumination. Note that, in the case of an applied bias, this potential is subtracted from the 1.23 V in Equation (1). In Equation (1), J_{sc} is the photocurrent density, η_F is the faradaic efficiency of the hydrogen evolution reaction, 1.23 V is the thermodynamic potential needed for water splitting at $T = 298$ K, and 1 atm and P_{light} are the power densities of the incident illumination, which hold only when the incident illumination matches the air mass global (AM 1.5 G). While the primary use of this equation is to determine the solar-to-hydrogen conversion efficiency, this equation can be extended to other solar-to-fuel conversions, such as the CO_2 reduction reaction, where various fuel products are expected. Thus, Equation (2) is a more universally applicable approach to calculate the solar-to-fuel conversion efficiency (η_{SFE}) [90]. In Equation (2), J_{OP} is the operational current density of a specific product, and V_{redox} is the thermodynamic potential for substrate-to-fuel conversion. It is worth mentioning that this metric is more complicated to use during CO_2 reduction reactions, as parameters such as faradaic efficiency and current density of specific products are required, but can be very complex to extract.

The applied bias photon-to-current efficiency (ABPE) is a metric derived from the STH efficiency with a notable adjustment that the ABPE uses an applied external potential (bias) to drive the chemical reaction of interest and is thus expressed according to Equation (3) [90]. In Equation (3), V_{app} is the applied potential used to drive the chemical transformation.

One essential metric of the performance of a solar cell is the overall solar-to-electrical energy conversion efficiency (η) that is determined by the open-circuit photovoltage (V_{oc}), the photocurrent density measured at a short-circuit current (J_{SC}), the fill factor (FF), and the intensity of the incident light (P_{in}), Equation (4) [91]. The fill factor can be determined by dividing the maximum power of the solar cell per unit area by J_{SC} and V_{OC} according to Equation (5) [91]. The fill factor ranges between 0 and 1 and the maximum power P_{max} can be calculated from the product of the open-circuit photovoltage and the photocurrent at the maximum power output.

An additional metric used to determine the efficiency of a DSSC or a DSPEC is incident photon-to-current conversion efficiency (IPCE) which determines the photocurrent obtained per incident photon flux as a function of monochromatic illumination. The IPCE can be written according to Equation (6), where the numerator describes the number of electrons generated per incident photon absorbed by the device at a particular wavelength (P_λ) [90]. In Equation (6), J is the photocurrent density, h is Planck's constant, c is the speed of light, e is the charge of the electron, and λ is the wavelength of irradiation. It is useful to correlate the IPCE to the key features of the DSPEC device working principle, that is, IPCE can also be expressed as a function of light harvesting efficiency (LHE), injection quantum yield (ϕ_{inj}), and the electron collection efficiency (η_c) as described in Equation (7) [92]. The injection quantum yield (ϕ_{inj}) of the photogenerated electron from the excited state of the photosensitizer to the conduction band of a semiconductor is determined by the ratio of the rate constant of electron injection (k_{inj}) and the sum of the excited-state deactivation rate constants (k_i) according to Equation (8) [92].

28359399, 0, Downloaded from https://onlinelibrary.wiley.com/doi/10.1002/ece2.70001, Wiley Online Library on [09/03/2025]. See the Terms and Conditions (https://onlinelibrary.wiley.com/terms-and-conditions) on Wiley Online Library for rules of use; OA articles are governed by the applicable Creative Commons License

Finally, like catalytic reactions, solar fuel production is often quantified in terms of turnover number (TON) and turnover frequency (TOF). The TON can be defined as the number of moles of the desired product divided by the number of mole of an active catalyst, Equation (9) [93].

It is worth to point out that not all catalyst molecules are active at the same time and that only a small proportion of them are activated during the charge transfer process and that those are the only ones that convert reactants into desired products. Thus, a more precise definition of TON was introduced by Savéant and coworkers as "*the TON specifies the maximum use that can be made of a catalyst for a special reaction under defined reaction conditions by the number of molecular reactions or reaction cycles occurring at the reactive center up to the decay of activity*" [93]. Similarly, turnover frequency (TOF) "*measures the instantaneous efficiency of the catalyst, and it can be derived from the number of the turnovers of the catalytic cycle with respect of the time per active site*" [94]. This can be written as Equation (10).

2.4 | Iron-Based Photosensitizers for the Development of Photoelectrodes

Most photosensitizers used for DSSCs and DSPECs applications are based on scarce metals such as ruthenium. However, some notable examples exist of DSSCs using organic photosensitizers and photosensitizers based on copper [95–98]. The number of reports that use iron photosensitizers is lower still [99–102] and is limited to DSSCs. Although iron complexes have been used as a redox mediator in DSPEC-type applications [85, 103], there are, to the best of our knowledge, currently no reported DSPEC relying solely on iron photosensitizers. This is due to the photophysics of iron PS, which includes extremely fast deactivation of the iron photosensitizer excited states, alongside redox potentials unsuitable to drive these challenging reactions. Yet, there has been tremendous efforts by pioneers in the field that managed to develop operative DSSCs using iron photosensitizers [99–102, 104–110]. The structures of these iron photosensitizers are shown in their respective sections and the metrics of the resulting DSSCs are tabulated in Table 1. This table illustrates the photovoltaic characteristics of iron-sensitized DSSCs documented in the literature, alongside their respective redox potentials, when available. Note that the photophysics of iron photosensitizers and their use in photoredox catalysis in solution has been recently reviewed [119] and will thus only be very briefly presented (Figure 3).

Light excitation of Fe(II) photosensitizer like the prototypical $[Fe(bpy)_3]^{2+}$ leads to the formation of the singlet metal-to-ligand charge transfer (^{1}MLCT) excited state (Figure 3). This state is usually represented as a formally oxidized metal center, with one electron removed from the t_{2g} orbitals, and a formally reduced ligand, with one electron added to the π^* orbital. This excited state is extremely short-lived and is converted on a ~100-fs time scale to low-lying metal-centered ligand-field states of the iron core, populating a high-spin quintet excited state ($^5T_{2g}$), with two electrons in the e_g orbitals and four electrons in the t_{2g} orbitals [120–123]. Thus, this very fast deactivation process prevents the formation of long-lived charge separated MLCT excited states that have made the reputation of other photosensitizers, like $[Ru(bpy)_3]^{2+}$. The main difference between these two MLCT photosensitizers stems from the final excited-state character, that is, ^{3}MLCT in the case of $[Ru(bpy)_3]^{2+}$ and metal-centered in the case of $[Fe(bpy)_3]^{2+}$, respectively. This decreases the energy available for excited-state electron injection or for any photocatalytic applications [124, 125].

2.5 | Fe(II) Analogs to Ru(II) Dyes and N-Heterocyclic Carbene (NHC)-Based Photosensitizers

The first report of iron-based photosensitizers in DSSCs dates back to 1998 and 2000 when Ferrere and Gregg used **Fe-1** (Figure 4) and a series of its derivatives immobilized on TiO_2 via anchoring groups such as diphosphonate, methyl-phosphonate, diethyl-methyl-phosphonate, and hydroxymethyl [99, 100]. The introduction of the strong field CN ligands allowed to destabilize the MC state and further increase visible light absorption. These photosensitizers had a low photoconversion efficiency due to the short-lived MLCT states of Fe(II) polypyridine-type photosensitizers which led to the ultrafast population of the metal centered (MC) states and subsequent ground-state recovery. Despite its poor excited-state properties, **Fe-1** generated an open-circuit photovoltage of −360 mV and a short-circuit photocurrent of 290 μA cm^{-2} under approximately one sun irradiation (75 mW cm^{-2}, $\lambda > 400$ nm). Regarding the other derivatives of **Fe-1**, their actual photocurrents, photovoltages, or efficiencies were not reported by the authors [99, 100].

The next breakthrough took another decade and originated from two pioneers in the field, Gros [101] and Wärnmark [102]. In 2013, Wärnmark and coworkers first reported the synthesis of an unfunctionalized NHC-carbene iron(II) complex. This NHC scaffold was introduced to destabilize the MC states relative to the MLCT states. At the time, the excited state was attributed to an MLCT state with a lifetime of 9 ps [126]. Very recently, it was shown that light excitation formed a ^{3}MLCT excited state that converted to the corresponding ^{3}MC excited-state manifold on a sub-100 fs time scale [127]. It is that ^{3}MC excited-state manifold that actually exhibits an excited-state lifetime between 10 and 20 ps, and not the MLCT state. Nevertheless, at the time, this report represented a significant discovery in the field of Fe(II)-based photosensitizers and it was only 2 years later that Wärnmark [102] and Gros [101] independently published their works on the N-heterocyclic NHC-carbene iron(II) complex (**Fe-2**) bearing a COOH anchoring group. Wärnmark and coworkers showed that **Fe-2** was able to inject electrons from the MLCT state to the conduction band of TiO_2 with an injection quantum yield of 92%. However, they did not report photovoltaic performances [102]. At the same time, Gros and coworkers showed that **Fe-2** could be efficiently anchored at the surface of TiO_2 and compared it to **Fe-3** [101]. The complexes were characterized by UV–Vis spectroscopy and cyclic voltammetry in acetonitrile. **Fe-2** displayed two MLCT transitions in the visible region: one involving the carbene units whose energy (380 nm) remained unchanged and the other, at lower energies, involving the central pyridine ring, which was sensitive to electronic tuning. Compared to **Fe-3** (λ_{max} MLCT = 560 nm), the carbene-based complex (**Fe-2**) showed blue-shifted MLCT transitions.

28359399, 0, Downloaded from https://onlinelibrary.wiley.com/doi/10.1002/ece2.70001, Wiley Online Library on [09/03/2025]. See the Terms and Conditions (https://onlinelibrary.wiley.com/terms-and-conditions) on Wiley Online Library for rules of use; OA articles are governed by the applicable Creative Commons License

TABLE 1 | Solar cell characteristics of iron-sensitized DSSCs [99–102, 104–118], using FTO as a conductive oxide, TiO_2 as a semiconductor, Pt as the counter electrode, and under AM 1.5 G simulated light source, unless otherwise mentioned.

Fe-Ps	Open-circuit photovoltage, V_{oc} (mV)	Short-circuit current, J_{sc} (mA cm^{-2})	Fill factor, FF	Efficiency, PCE (%)	E_{ox} (V vs. NHE)	E_{red} (V vs. NHE)	Ref
Fe-1	−360	0.290	—	—	—	—	[100]
Fe-2	457	0.41	0.68	0.13	1.09	−1.11	[101]
Fe-2	450	5.27 ± 0.14	0.55	1.30 ± 0.07	0.91	—	[104]
Fe-2	466	2.09 (1.9 ± 0.2)	0.75	0.73	0.85	−1.08	[105]
Fe-2 + Fe-19	420	8.63 ± 0.24	0.55	1.98 ± 0.1	—	—	[104]
Fe-3	250	0.0016	0.50	0.01	1.45	−0.81	[101]
Fe-4	368	0.12	0.71	0.03	1.55	−0.99	[106, 107]
Fe-5	400	0.33	0.73	0.10	1.06	−1.10	[106, 107]
Fe-5	490	3.95	0.61	1.18	1.06	—	[108]
Fe-6	440	0.36	0.73	0.11	1.05	−1.09	[106, 107]
Fe-7	390	0.36	0.71	0.10	1.06	−1.10	[106, 107]
Fe-8	440	3.55	0.60	0.94	0.98	—	[108]
Fe-9	460	2.69	0.63	0.78	0.94	—	[108]
Fe-10	470	6.03	0.59	1.68	0.94	—	[109]
Fe-11	430	6.07	0.61	1.58	0.92	—	[109]
Fe-12	470	5.81	0.57	1.56	0.93	—	[109]
Fe-13	390	6.11	0.49	1.17	0.76	—	[109]
Fe-14	470	6.80	0.57	1.83	0.88	—	[109]
Fe-15	350	5.20	0.61	1.11	0.89	—	[109]
Fe-16	512	3.52 (3.3 ± 0.2)	0.72	1.31	0.8	−1.75	[105]
Fe-17	416	3.23 (2.1 ± 0.4)	0.69	0.93	0.82	−1.67	[105]
Fe-18	390	7.84 ± 0.38	0.56	1.71 ± 0.15	0.83	—	[104]
Fe-19	390	6.64 ± 0.12	0.59	1.52 ± 0.10	0.82	—	[104]
Fe-20	582 ± 2	3.7 ± 0.2	0.59	1.3 ± 0.1	—	—	[110]
Fe-21	570 ± 3	2.4 ± 0.1	0.53	0.7 ± 0.1	—	—	[110]
Fe-22	763	0.41	0.35	0.10		+0.85	[111]
Fe-23	841	0.039	0.28	9.1×10^{-3}		+1.11	[111]
Fe-24	593	0.606	0.58	0.211		—	[112]
Fe-25	601	0.776	0.52	0.246		—	[112]
Fe-26	191	0.036	0.50	0.0034			[113]
Fe-27	491	0.132	0.63	0.0412			[113]
Fe-28	710	12.91	0.64	5.88	1.35	+1.12	[114]
Fe-29	690	9.21	0.63	4.04	1.30	+1.16	[114]
Fe-30	632	9.39	0.61	3.61	1.36	+0.024	[115]
Fe-31	652	9.93	0.68	4.39	1.45	−0.20	[115]
Fe-32	667	11.25	0.63	4.76	1.15	+0.22	[115]
Fe-33	633	13.15	0.61	5.05	1.29	+0.04	[115]
Fe-34	666	7.94	0.64	3.36	1.35	−0.02	[115]
Fe-35	684	6.08	0.67	2.79		+0.35	[116]
Fe-36	664	5.13	0.67	2.30		+0.35	[116]
Fe-37	656	4.44	0.66	1.95		+0.35	[116]

28359399, 0, Downloaded from https://onlinelibrary.wiley.com/doi/10.1002/ece2.70001, Wiley Online Library on [09/03/2025]. See the Terms and Conditions (https://onlinelibrary.wiley.com/terms-and-conditions) on Wiley Online Library for rules of use; OA articles are governed by the applicable Creative Commons License

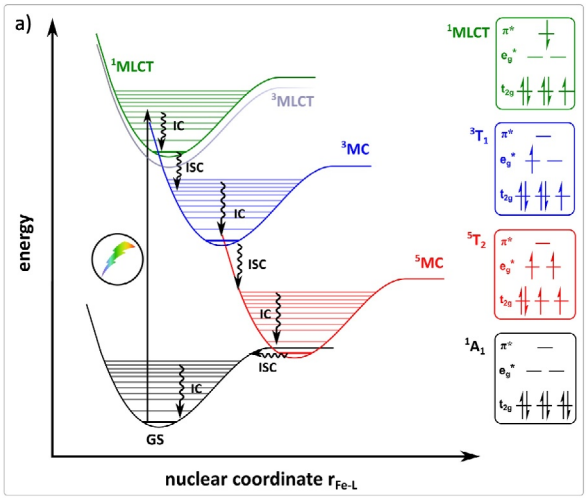


FIGURE 3 | Schematic potential energy surfaces and relevant electronic states for the excited-state decay of Fe(II)-based photosensitizers. Electron configurations are given for Oh symmetry for simplicity. Radiative decay pathways are denoted as dotted straight lines, whereas nonradiative decay pathways are presented as wavy lines. GS = ground state, IC = internal conversion, ISC = intersystem crossing, MC = metal-centered, MLCT = metal-to-ligand charge transfer. Reprinted with permission from reference [119]. Copyright Elsevier 2024.

The cyclic voltammogram of **Fe-2** showed a reversible oxidation wave for the Fe(III)/Fe(II) couple at 1.09 V versus NHE, which is an important characteristic for the ground-state regeneration of the oxidized dye by the redox mediator. For comparison, the oxidation potential of **Fe-3** was found to be 1.45 V versus NHE, in good agreement with the lower σ-donor character of the ligand and the lack of carbene-based π*-orbitals that is present in **Fe-2** [101]. The incident photon to electron conversion efficiency for **Fe-2** was 2.5% IPCE, whereas **Fe-3** did not show any significant conversion. Other parameters, such as short-circuit photocurrent density of 0.41 mA cm^{-2}, open-circuit photovoltage of 457 mV, fill factor of 0.68, and overall efficiency of 0.13% obtained for **Fe-2** all indicated a better performance than its terpyridine analog **Fe-3**. It is worth mentioning that, in the case of **Fe-2** (Table 1, entry 3) used by Gros and coworkers [104], a customized electrolyte containing a mixture of Li^+, Mg^{2+}, TBAI (tetrabutylammonium iodide), and GuNCS (guanidine thiocyanate) was used. The authors used these additives to improve charge injection and decrease the open-circuit photovoltage (V_{oc}). In addition, the GuNCS is assumed to absorb onto the TiO_2 and reduce recombination with the I_3^- redox mediator and hence slightly improve the fill factor and the open-circuit photovoltage. Wärnmark and coworkers used **Fe-2** (entry 4) co-adsorbed with chenodeoxycholic acid to ensure full coverage of the TiO_2 surface and minimize charge recombination with the I_3^-/I^- electrolyte [105].

Transient absorption spectroscopy was used to gain insights into the excited-state dynamics of **Fe-2** and **Fe-3** in acetonitrile solutions [101]. Pulsed-light excitation of **Fe-3** led to the formation of ^{1,3}MLCT states that decayed on the 100–200 fs time scale to the $^5T_2$ state, as indicated by the disappearance of [1, 3] MLCT excited-state absorption (ESA) in the 380–460 nm range and above 600 nm. The $^5T_2$ state was characterized by a sharp absorption at 355 nm and bleaches at 574 and 342 nm. The lifetime of the $^5T_2$ state was determined as 2.2 ns. On the other hand, the absorption changes of **Fe-2** led to a broad positive ESA between 320 and 360 nm as well as between 420 and 450 nm and at wavelength greater than 580 nm. These three excited-state absorption features are characteristic of the ^{3}MLCT state of Fe(II) NHC complexes. The MLCT transition also led to the corresponding transient bleach of the ground-state transitions (GSB), peaking at 400 and 505 nm. The positive ESA and negative GSB traces are almost mirror images for **Fe-2**, which was not the case for **Fe-3** due to the population of the $^5T_2$ state. Wärnmark and coworkers also studied the kinetics of electron transfer processes of **Fe-2** anchored on TiO_2 [102]. These measurements took place in MeCN as well as on Al_2O_3 with 80 fs time resolution to distinguish the effects of the –COOH group and surface immobilization from electron injection. Based on the spectra and the kinetics, when **Fe-2** was excited at 485 nm in MeCN, a major 18 ps component was determined and assigned to the excited-state lifetime of the ^{3}MLCT state. A minor 7 ps component was also determined and attributed to vibrational cooling. As they observed, the prolongation of the ^{3}MLCT lifetime was attributed to the stabilization of the ^{3}MLCT state, as the MC states were expected to be almost unaffected by the –COOH substitution. The transient absorption spectra of **Fe-2** anchored on Al_2O_3 showed similar features as those recorded in acetonitrile and two main deactivation processes were determined, the excited-state decay of the ^{3}MLCT that occurred in 37 ± 3 ps and the vibrational cooling that occurred in 1.0 ± 0.1 ps. Although all the signals decayed in less than 100 ps for **Fe-2** in solution or anchored on Al_2O_3, the kinetics were drastically longer when anchored on TiO_2. They were however much more complicated as four components were needed to fit the data, with rates of 4 ± 3 ps, 30 ± 15 ps, 149 ± 67 ps, and > 10 ns. The spectra profiles of the components resembled both the oxidized photosensitizer as well as the excited state and it was thus complicated to disentangle the respective contribution. Nevertheless, the appearance of signal decaying with time constants greater than 100 ps is in line with efficient electron injection. In combination with other techniques, it was shown that the **Fe-2** exhibited a 92% yield of conversion of photons to injected electrons, but unfortunately a large portion of the injected electrons underwent fast electron-cation recombination [102].

In 2016, Pastore et al. [107] provided an overview of the photovoltaic characteristics of heteroleptic Fe(II)-carbene sensitized photoanodes using **Fe-5**, **Fe-6**, and **Fe-7** as well as homoleptic complexes **Fe-2** and **Fe-4**. **Fe-5** was an analog of the benchmark carbene complex **Fe-2,** whereas **Fe-6** and **Fe-7** had additional electron donating substituents, that is, anisyl and triphenylamine, respectively. **Fe-6** and **Fe-7** were designed to introduce and increase the polarization of the photosensitizer in its excited state, thereby enhancing the electron transfer properties while maintaining the photogenerated hole away from the semiconductor surface to reduce recombination processes from injected electrons. All the complexes were characterized by UV–Vis spectroscopy in acetonitrile. As mentioned before, while **Fe-2** complex exhibits two MLCT transitions in the visible region at 394 and 520 nm, **Fe-4** exhibits an MLCT transition at 501 nm. Also, compared to **Fe-2**, an additional MLCT band was observed for **Fe-5**, **Fe-6,** and **Fe-7** at 430 nm which was attributed to

28359399, 0, Downloaded from https://onlinelibrary.wiley.com/doi/10.1002/ece2.70001, Wiley Online Library on [09/03/2025]. See the Terms and Conditions (https://onlinelibrary.wiley.com/terms-and-conditions) on Wiley Online Library for rules of use; OA articles are governed by the applicable Creative Commons License

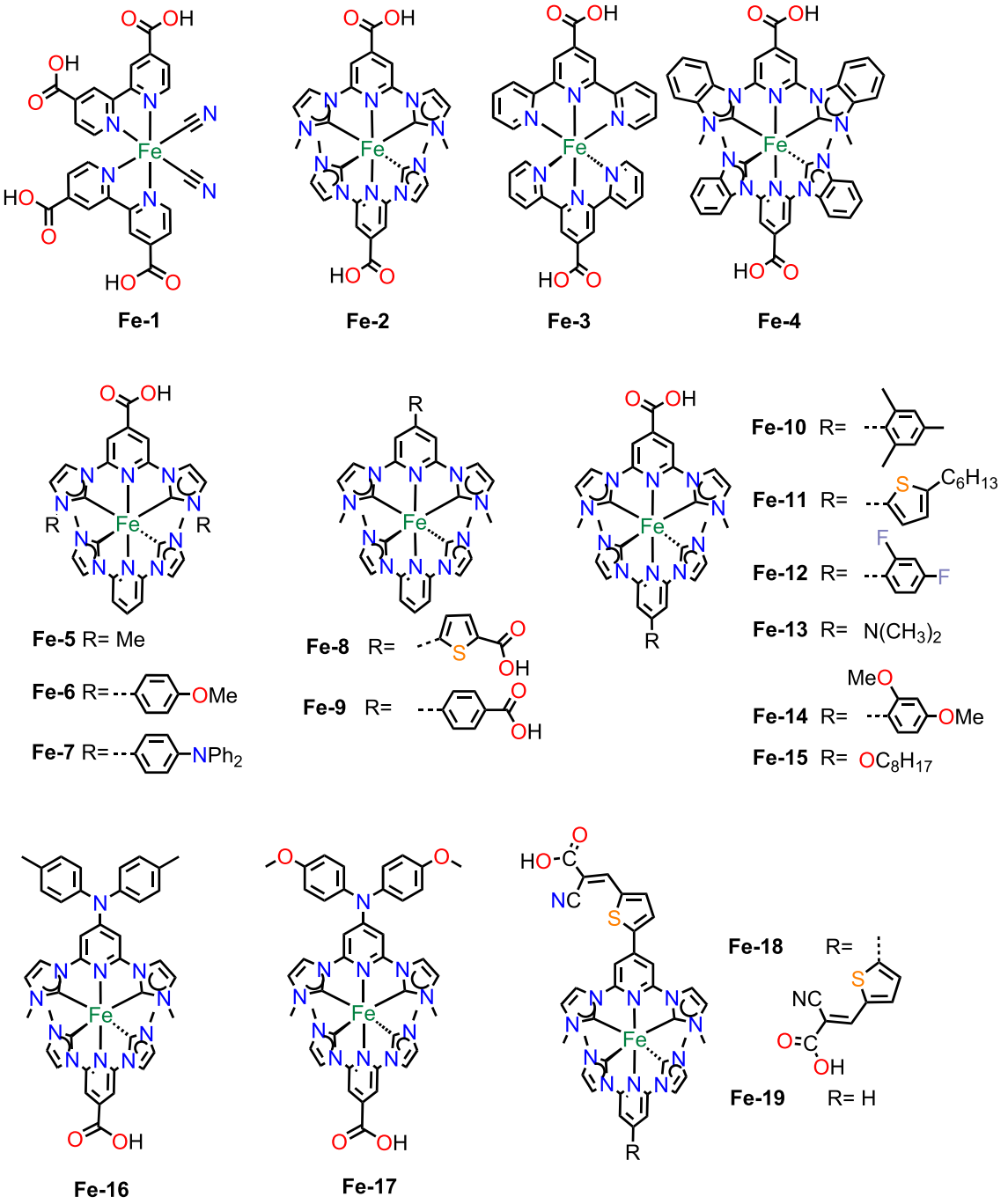


FIGURE 4 | Structures of Fe(II) analogs to Ru(II) dyes and N-heterocyclic carbene (NHC)-based photosensitizers anchored on TiO_2 for DSSC applications [99–102, 104–109].

MLCT transition from the iron center to the unsubstituted pyridine of the ligand scaffold with molar absorption coefficients that ranged from 5 075 to 8 540 $M^{-1}cm^{-1}$. Cyclic voltammetry was carried out in acetonitrile using 0.1 M Bu_4NPF_6 as an electrolyte at 100 mV s^{-1}. **Fe-2** and **Fe-4** displayed a reversible oxidation wave of the Fe(III)/Fe(II) couple at 1.09 and 1.55 V versus NHE, respectively, which showed favorable thermodynamics for dye regeneration by the I_3^-/I^- redox mediator used in this study. The oxidation potentials of **Fe-5**, **Fe-6,** and **Fe-7** were also found around 1.06 V versus NHE (Table 1). The first reduction of **Fe-2**, **Fe-4**, **Fe-5**, **Fe-6**, and **Fe-7** occurred at −1.11, −0.99, −1.10, −1.09, and −1.10 V versus NHE, respectively [106, 107]. In addition, the authors provided an overview of the photovoltaic characteristics of heteroleptic Fe (II)-carbene sensitized photoanodes using **Fe-5**, **Fe-6**, and **Fe-7** as well as homoleptic complexes **Fe-2** and **Fe-4**. The IPCE at 500 nm was reported as 3% and 2.5% for **Fe-6** and **Fe-5**, respectively. The photocurrent density (J_{sc}) ranged between 0.33 and 0.36 mA cm^{-2} for complexes **Fe-5**, **Fe-6**, and **Fe-7**. Complexes **Fe-5**, **Fe-6**, and **Fe-7** exhibited lower V_{oc} values of around 400–450 mV (Table 1) compared to standard photosensitizers like N719 Ru(II), which typically exhibits V_{oc} values around 690 mV. This decrease in open-circuit photovoltage and photocurrent in the dyes can again be attributed to an

28359399, 0, Downloaded from https://onlinelibrary.wiley.com/doi/10.1002/ece2.70001, Wiley Online Library on [09/03/2025]. See the Terms and Conditions (https://onlinelibrary.wiley.com/terms-and-conditions) on Wiley Online Library for rules of use; OA articles are governed by the applicable Creative Commons License

unfavorable balance between interfacial electron injection and the recombination pathway. Ultrafast transient absorption spectroscopy was reminiscent of those previously described for **Fe-2** with a GSB at 400 and 505 nm and positive ESA between 320 and 360 nm as well as between 420 and 450 nm and at wavelength greater than 580 nm [107]. Certainly, the absorption maxima for complexes **Fe-3** and **Fe-4** are blue-shifted by 20 nm compared to **Fe-2** and unfunctionalized NHC-carbene Fe(II) complex. The addition of the two carboxylic acid groups led to the stabilization of the t_{2g} system upon π back-donation from the iron center. The effect of the number of –COOH groups on the photophysical properties was also examined with complex **Fe-5**, which was functionalized with the –COOH group on only one ligand. The absorption spectrum of **Fe-5** exhibited one additional band at 440 nm that was assigned to the charge transfer transition between the metal and the pyridine ring without the carboxylic group. The lowest-energy band at 510 nm was attributed to an MLCT transition involving the pyridine bearing the carboxylic group and the band at 380 nm was the signature of the Fe-carbene MLCT transition, which is not affected by the presence of the carboxylic group. Overall, complexes **Fe-2** to **Fe-5** highlighted the action of two effects induced by the ligand design. The first one was the stabilization of the MLCT levels due to the introduction of electron-accepting groups (**Fe-4**, **Fe-5**) and the second was the additional downshift of the MLCT states, most probably due to an increased π back-donation. Complexes **Fe-6** and **Fe-7** with different donor groups in combination with –COOH anchoring groups were expected to improve the vectorial electronic charge transfer into the semiconductor and limit the possible recombination reactions by keeping the progenerated hole far from the semiconductor surface. Hence, through the femtosecond transient spectroscopy, complexes **Fe-6** and **Fe-7** followed the same relaxation scenario as **Fe-5**, with similar ^{3}MLCT lifetimes of 10 and 12 ps, respectively, which are still long enough to expect PCE values > 0.1% [107].

In 2021, Reddy Marri et al. reported three Fe(II) pyridyl-NHC-carboxylic heteroleptic complexes with a thiophene (**Fe-8**) or a phenyl (**Fe-9**) spacer, or without spacer (**Fe-5**) between the pyridine and the –COOH anchoring group [108]. The spacer was introduced to increase the distance between the TiO_2 surface and the iron center in order to decrease the undesired recombination processes. All the complexes were characterized with UV–Vis spectroscopy and cyclic voltammetry. The UV–vis spectra were consistent with the typical NHC–carbene iron complexes with the observation of a higher energy band (250–330 nm) and two other MLCT bands (340–600 nm). Electrochemical measurements highlighted that the introduction of thiophene (**Fe-8**) or phenyl (**Fe-9**) spacer slightly decreased the oxidation potentials to 0.98 and 0.94 V, respectively, with respect to **Fe-5** (1.06 V vs. NHE) [108]. The increase in molar absorption coefficients due to extended π conjugation induced by the thiophene moiety in **Fe-8** was used to explain the higher power conversion efficiency (PCE) of approximately 0.94% achieved by this complex, with a photocurrent density (J_{sc}) of 3.55 mA cm^{-2} and open-circuit photovoltage (V_{oc}) of 440 mV, leading to a fill factor of 0.60. **Fe-9** had an efficiency of 0.78% along with J_{sc} of 2.69 mA cm^{-2}, V_{oc} of 460 mV, and FF of 0.63. However, **Fe-5** demonstrated overall better results, with a PCE of 1.2% and an optimal combination of photocurrent 3.95 mAcm^{-2}, open-circuit photovoltage of 490 mV, and FF of 0.61. Although the complexes with conjugated spacers **Fe-8** and **Fe-9** exhibited larger absorption in the UV–Vis region, these complexes exhibited lower performance than the nonconjugated complex **Fe-5**.

Similar studies were conducted on a series of six photosensitizers (**Fe-10**–**15**) in which **Fe-10**–**12** have the pyridine ring bearing an aromatic moiety (Figure 4), whereas **Fe-13** and **Fe-15** have a dimethyl amine and O-octyl group, respectively [109]. The photophysical data were in line with those reported for this type of complexes. In the lowest-energy portion of the spectra, **Fe-10**–**12** and **Fe-14** complexes presented a broad and intense absorption, ranging from 410 to 600 nm, whereas **Fe-13** and **Fe-15** absorbed in a narrower window (450–600 nm). **Fe-11** showed the broadest and most red-shifted absorption at 501 nm thanks to the thiophene unit. Heteroatom-substituted complexes **Fe-13** and **Fe-15** exhibited two MLCT bands of similar intensities unlike the other complexes, attributed to strong heteroatom donating capability in N,N-dimethylamine and O-octyl groups, respectively. To study the thermodynamic properties of all dyes, cyclic voltammetry of TiO_2-sensitized thin films immersed in 0.1 M $LiClO_4$/acetonitrile electrolyte were carried out. The anodic scan revealed reversible Fe(III)/Fe(II) waves with potentials that ranged from 0.76 V versus NHE for the strong electron donor dimethylamine substituent in **Fe-13** up to 0.94 V versus NHE for **Fe-10**.

The cathodic shift is caused by the presence of donor groups like -OR either as substituents on the benzene ring (**Fe-14**, 0.88 V vs. NHE) or directly attached to the pyridine (**Fe-15**, 0.89 V vs. NHE). **Fe-14** led to the best efficiency of 1.83% using Mg^{2+} and NBu_4I-based electrolytes and a 20-μm thick TiO_2 layer. The magnesium cation was used to increase the electronic coupling between the photosensitizer and the conduction band of TiO_2 and also promoted further directionality of the MLCT excited state. This led to an increased excited-state charge injection while the tetrabutylammonium iodide allowed to decrease the cell resistance without lowering the potential of the conduction band of TiO_2. It was found that **Fe-14** exhibited a photocurrent density of 6.8 mA cm^{-2} and an open-circuit photovoltage of 0.47 V resulting in a power conversion efficiency of 1.83. The IPCE measurement with **Fe-12**, **Fe-13**, and **Fe-14** using 16 μm TiO_2 thickness ranged from 45% for **Fe-13** to over 60% for **Fe-14**.

In 2021, Lindh et al. reported the use of push–pull iron complexes with NHC carbene ligands [105]. **Fe-16** and **Fe-17** are heteroleptic complexes with one ligand bearing a carboxylic acid group for efficient surface anchoring while the second ligand was functionalized with biarylamine electron donating groups. These photosensitizers were compared to the reference **Fe-2**. Analysis of the structures by density functional theory (DFT) revealed that amine-substituted ligands destabilized both the highest occupied molecular orbital (HOMO) and lowest unoccupied molecular orbital (LUMO), whereas the use of carboxylic acid-substituted ligands (**Fe-16** and **Fe-17**) stabilized the LUMO of the iron complexes. As previously shown for these kind of Fe carbene complexes, **Fe-16** and **Fe-17** exhibited a double-peaked absorption band between 350 and 600 nm attributed to metal-to-ligand charge transfer. Electrochemically, **Fe-2** was found to display two redox events at 1.08 and −1.08 V versus NHE, highly

28359399, 0, Downloaded from https://onlinelibrary.wiley.com/doi/10.1002/ece2.70001, Wiley Online Library on [09/03/2025]. See the Terms and Conditions (https://onlinelibrary.wiley.com/terms-and-conditions) on Wiley Online Library for rules of use; OA articles are governed by the applicable Creative Commons License

consistent with those reported in 2015 [101, 102]. For **Fe-16**, electrochemical potentials of 0.8 and −1.75 V versus NHE were determined, whereas the potentials were 0.82 and −1.67 V versus NHE for **Fe-17** [105]. Chenodeoxycholic acid, a co-adsorbent, was introduced to further space the photosensitizers and mitigate charge recombination. Analysis of solar cell parameters revealed that the heteroleptic complexes **Fe-18** and **Fe-19** outperformed the homoleptic complex **Fe-2**. **Fe-16** exhibited the most significant improvement, achieving a maximum IPCE of 29% at 500 nm. Additionally, **Fe-16** showed an increase in photocurrent to over 3 mA cm^{-2} compared to 2 mA cm^{-2} for **Fe-2**, along with enhancements in V_{oc} of 512 mV which resulted in an enhanced overall efficiency. Conversely, **Fe-17** exhibited inferior performance compared to **Fe-16**, which was attributed to the presence of methoxy electron donating groups on the diphenyl amine substituent, leading to decreased V_{oc} of 400 mV compared to its methyl analog. Femtosecond TAS was used to investigate the interfacial charge transfer of complexes **Fe-16**, **Fe-17**, and **Fe-2** to TiO_2 mesoporous films in MeCN containing 0.1 M TBA methane-sulfonate and 0.1 M methane-sulfonic acid [105]. The amplitudes of the signal in the GSB region that persisted after 10 ns were 5% for **Fe-16**, 10% for **Fe-17**%, and 13% for **Fe-2**. This difference is evidence that **Fe-17** would have a larger fraction, compared to **Fe-16**, of the long-lived electrons injected into the TiO_2 electrode. For both **Fe-16** and **Fe-17**, transient absorption spectroscopy was enabled to detect ultrafast electron injection that occurred faster than 100 fs. However, ultrafast recombination between the injected electrons and the oxidized photosensitizer was also very efficient such that only 5%–10% of the initial excited photosensitizer actually contributed to the photocurrent [105].

In 2023, Gros and coworkers examined the performance of NHC carbene-Fe(II) complexes bearing thienylcyanoacrylic (ThCA) anchoring groups, **Fe-18** and **Fe-19**, with the aim to increase metal to surface charge separation and enhance the light harvesting window in iron-based DSSCs [92, 104]. The photophysical data were in line with those reported before for similar carbene-Fe(II) complexes. Nevertheless, the higher energy MLCT band (ca 340 nm) of these complexes (**Fe-18** and **Fe-19**) was masked by the very broad π-π^* characteristic absorption. The other MLCT band displayed a broad absorption ranging from 450 to 650 nm with the homoleptic **Fe-18** exhibiting the broadest and largest red-shifted absorption at 555 nm.

The red-shifted MLCT bands observed for **Fe-18** and **Fe-19** were found even more profound in the spectra of their TiO_2 thin films (ca. 13 μm thickness), and when a mixture of **Fe-18** and **Fe-2** was used, a panchromatic absorption was achieved reaching up to 700 nm. Interestingly, this red shift in UV–Vis absorption was consistent with the reduced electrochemical gap that was measured by cyclic voltammetry (see below) on the sensitized TiO_2 thin films in contact with 0.1 M $LiClO_4$ in acetonitrile solutions. On the titania substrates, both complexes, **Fe-18** and **Fe-19**, revealed a reversible oxidation potential at 0.83 and 0.82 V versus NHE, respectively, slightly more cathodic than that recorded for the standard **Fe-2** (0.91 V vs. NHE). In addition, these complexes were all featuring irreversible cathodic waves, with **Fe-18** and **Fe-19** displaying the first irreversible wave, which was absent in the reference **Fe-2**, at −0.64 and −0.70 V versus NHE, respectively. Based on these potentials, the authors estimated that the HOMO–LUMO gap provided values ranging between 650 and 833 nm which is consistent with the onset of the absorption found at around 700 nm for these complexes. The photovoltaic properties of these new complexes were examined using the previously customized electrolyte comprising Li^+, Mg^{2+}, TBAI, and GuNCS [104]. On transparent thin films with an active layer thickness of 13 μm, the incident photon to current conversion efficiency recorded in the customized electrolyte for the reference **Fe-2** was 45%, possibly due to its higher injection driving force, which was close to the one determined for **Fe-18** (40%) and larger than that of **Fe-19** (35%). When studied under AM 1.5 white light illumination, **Fe-18** demonstrated the best performance, exhibiting V_{oc} of 0.37 V, FF of 0.56, and photocurrent density of 6.23 mA cm^{-2} along with the highest power conversion efficiency of 1.28%. Similarly, **Fe-19** displayed a photocurrent density of 5.30 mA cm^{-2}, slightly smaller than **Fe-18**, and a power efficiency of 1.14%, both still performing better than the reference COOH-based **Fe-2** dye with a photocurrent density of 4.64 mA cm^{-2} and a power conversion efficiency of 1.11% measured under the same conditions. The lower performance obtained for **Fe-2** is in agreement with its narrowest spectral response compared to **Fe-18** and **Fe-19**. The performances of these complexes were further investigated by increasing the thickness of TiO_2 up to 20 μm with a top scattering layer of approximately 100 nm anatase nanoparticles with the aim of improving the light harvesting capability of the photosensitizers. Under these conditions, slightly enhanced performances were observed with photocurrent reaching up to 8, 7, and 5 mA cm^{-2} for **Fe-18**, **Fe-19**, and **Fe-2**, respectively, with a respective power conversion efficiency of 1.71%, 1.52%, and 1.30%. The slightly lower performance of **Fe-19** compared to **Fe-18** was attributed to its lower injection quantum yield and faster recombination rate with I_3^- which was evidenced by the less negative threshold of the dark current. Finally, a system composed of a combination of both **Fe-2** and **Fe-18** deposited on 20 μm thick TiO_2 generated an enhanced performance with J_{sc} of 9 mA cm^{-2}, V_{oc} of 0.42 V, and a PCE of 2%, representing the best efficiency ever reported for n-type sensitization by Fe(II) dyes [104].

2.6 | Ferrocene-Based Photosensitizers and Other Derivatives

Ferrocene-based complexes have attracted significant attention for DSSC applications. Intuitively, ferrocene can act as a photosensitizer by absorbing the blue region of the solar spectrum, but it can also act as a stable redox mediator. Ferrocene has thus been efficiently used in the development of "push–pull" architectures, providing good electronic communication through intramolecular charge transfer (ICT), thus leading to larger spatial charge separation. The absorption and ICT character can be tuned by introducing substituents on the ferrocenyl backbone, for example. Overall, its stability and reversible redox properties make ferrocene a valuable component in the development of advanced materials for solar energy conversion, organic photovoltaics, and other light-based technologies [128].

El Zohry and coworkers developed two photosensitizers based on ferrocene derivatives, **Fe-20** and **Fe-21** (Figure 5) [110].

28359399, 0, Downloaded from https://onlinelibrary.wiley.com/doi/10.1002/ece2.70001, Wiley Online Library on [09/03/2025]. See the Terms and Conditions (https://onlinelibrary.wiley.com/terms-and-conditions) on Wiley Online Library for rules of use; OA articles are governed by the applicable Creative Commons License

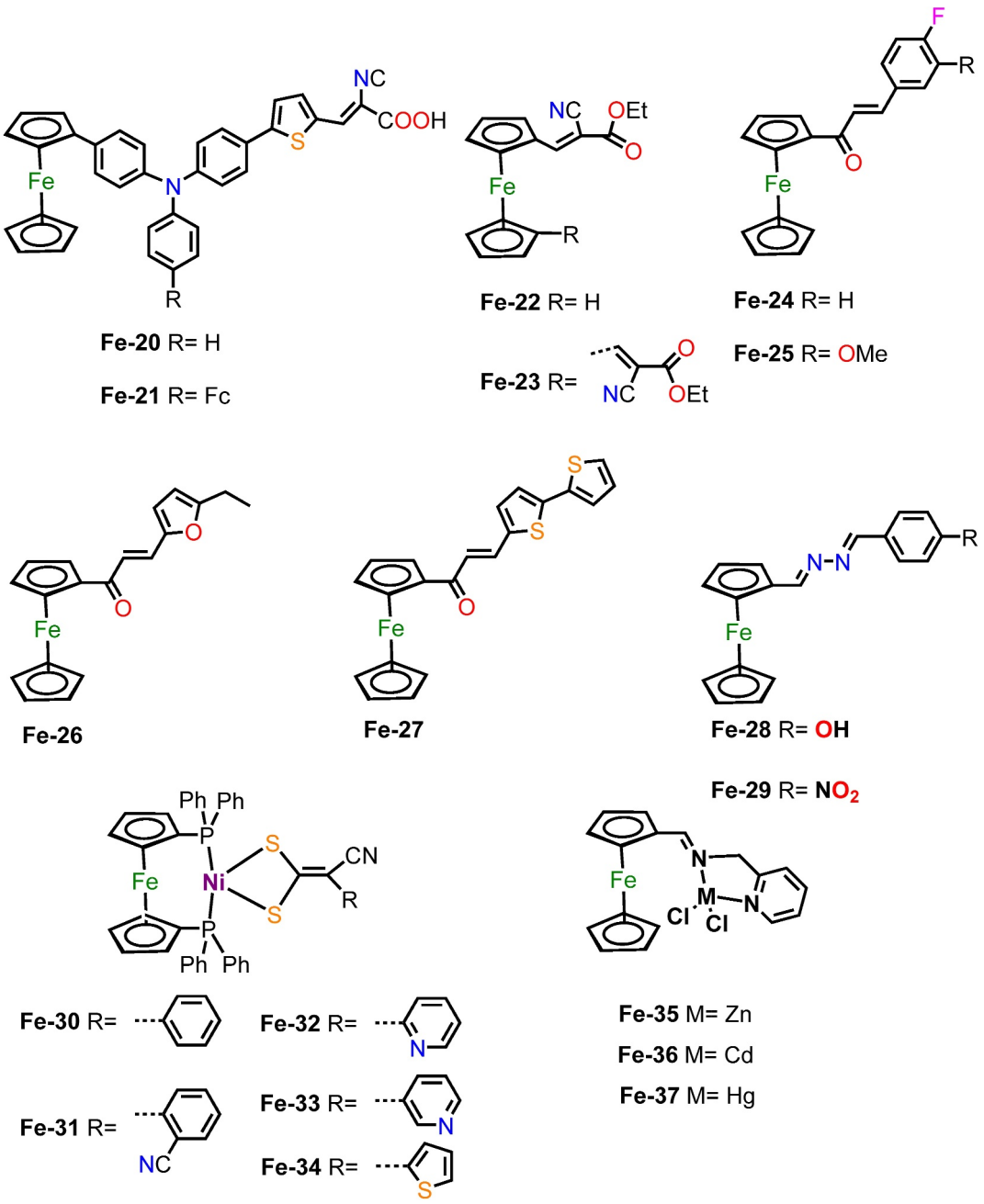


FIGURE 5 | Structures of ferrocene-based photosensitizers and other Fe(III) analogs that were used for DSSC applications [110–118].

These photosensitizers operated with efficiencies of 1.3% and 0.7%, respectively, compared to 5.5% for ferrocene only. The primary factor contributing to the decreased efficiency of **Fe-20** and **Fe-21** was their lower photocurrent density, as indicated in Table 1. Additionally, the IPCE value for ferrocene exceeded that of ferrocene-modified dyes **Fe-20** and **Fe-21**. Further investigation was conducted using electrochemical impedance spectroscopy (EIS) to elucidate the electron transfer processes within the solar cells. **Fe-20** and **Fe-21** exhibited greater resistance to recombination loss between electrons in the conduction band of TiO_2 and the mediator, an observation that was attributed to faster recombination with the ferrocene core. The inclusion of chenodeoxycholic acid was noted to mitigate recombination in the presence of ferrocene, resulting in increased photocurrent and open-circuit photovoltage of the device. Consequently, optimizing these parameters could enhance the photovoltaic performance of solar cell devices, leading to improved efficiency [110].

In 2018, Ghosh et al. reported two new ferrocene-based cyanovinyl dyes, **Fe-22** and **Fe-23** [111]. These dyes are only different by the number of donor–acceptor cyanovinyl groups, with **Fe-22** bearing a single cyanovinyl group and **Fe-23** bearing two cyanovinyl groups. Both **Fe-22** and **Fe-23** absorb light in a wide range of the solar spectrum due to these donor–acceptor groups. The thin film-based absorption spectra of both dyes showed wide absorption in the visible region spanning 400–700 nm. The electrochemical properties were studied in acetonitrile solutions using a 0.1-M tetrabutylammonium perchlorate electrolyte. **Fe-22** exhibited a reversible redox process at +0.85 V

28359399, 0, Downloaded from https://onlinelibrary.wiley.com/doi/10.1002/ece2.70001, Wiley Online Library on [09/03/2025]. See the Terms and Conditions (https://onlinelibrary.wiley.com/terms-and-conditions) on Wiley Online Library for rules of use; OA articles are governed by the applicable Creative Commons License

versus NHE attributed to a Fe(III)/Fe(II) redox couple. This potential was shifted positively to +1.11 V versus NHE for **Fe-23**. The resulting DSSC showed an open-circuit photovoltage of 763 and 841 mV as well as a photocurrent of 0.41 and 0.039 mA cm^{-2} for **Fe-22** and **Fe-23**, respectively, along with a fill factor of 0.35.

Arshad et al. reported two donor-π-acceptor ferrocenyl-chalcones where **Fe-24** served as the parent compound and **Fe-25** was further functionalized with a methoxy group in position three of the phenyl ring to enhance the donating character of the compound [112]. Both photosensitizers were composed of a central ferrocene derivative as the main donor, an enone group that acted as the π-bridging ligand and a fluorophenyl ring as electron acceptor unit. The additional methoxy group of **Fe-25** was found to enhance the backbone planarity of the compound and therefore improved intermolecular charge transfer (ICT). The addition of the methoxy group was also reflected in the DSSC efficiency parameters. The sensitization on TiO_2 was performed by dipping the TiO_2 coated FTO glass in the respective photosensitizer solution. This process occurred overnight and the samples were then rinsed with excess acetonitrile to remove poorly bound photosensitizers. **Fe-25** showed an open-circuit photovoltage of 601 mV, a photocurrent of 0.776 mA cm^{-2} and a moderate fill factor of 0.52, while **Fe-24** showed a lower open-circuit photovoltage and photocurrent of 593 mV and 0.606 mA cm^{-2}, respectively, but an improved fill factor of 0.58. This improved performance of **Fe-25** was attributed to the enhanced planarity of the photosensitizer, which promotes better electronic communication across the backbone of the compound, ultimately resulting in better conversion efficiency. Nevertheless, the overall efficiency were still extremely small, that is, 0.211% and 0.246% for **Fe-24** and **Fe-25**, respectively (Table 1).

In 2021, Anizaim et al. reported two new ferrocenyl-chalcones photosensitizers, **Fe-26** and **Fe-27**, where the ferrocene unit is linked to a 5-ethylfuran-2-yl moiety (**Fe-26**) or to a bithiophene-5-yl moiety (**Fe-27**) [113]. Based on X-ray structural analysis, **Fe-27** showed more improvement in structure planarity compared to **Fe-26** which had a slightly twisted structure. To fabricate the photoelectrode, acetonitrile solutions of the photosensitizers and chenodeoxycholic acid (10:1) were drop casted onto the TiO_2 thin films. Both photosensitizers exhibited broad absorption bands at 486 and 483 nm for **Fe-25** and **Fe-27**, respectively, in addition to more intense π-π* transition band at 345 nm for **Fe-26** that was red-shifted to 385 nm for **Fe-27**. **Fe-26** exhibited a photocurrent of 0.036 mA cm^{-2} and an open-circuit photovoltage of 191 mV with a fill factor of 0.50 resulting in an overall efficiency of 0.0034%. **Fe-27** showed an improved photocurrent of 0.132 mA cm^{-2}, an open-circuit photovoltage of 491 mV, and a fill factor that reached 0.63, leading to an overall efficiency of 0.0412%, that is, a 1-fold enhancement compared to **Fe-26**.

Singh et al. used two other ferrocene-based dyes, **Fe-28** and **Fe-29**, that were composed of an extended conjugated π-system, with an azene spacer (CH=N–N=CH) linked to a phenolic (**Fe-28**) or nitrophenyl (**Fe-29**) group as the terminal anchoring group [114]. The UV–Vis absorption spectra of **Fe-28** and **Fe-29** showed a broad absorption band at 506 and 474 nm, respectively, attributed to d-d transition. The electrochemistry of both photosensitizers was studied in dichloromethane with 0.1 M tetrabutylammonium perchlorate as the supporting electrolyte. The cyclic voltammetry of **Fe-28** and **Fe-29** showed onset oxidation potential of +1.35 and +1.30 V versus NHE and onset reduction potential of +1.12 and +1.16 V versus NHE, respectively. Photovoltaic data for the two complexes showed that the phenolic complex (**Fe-28**) exhibited a better cell performance with a photocurrent of 12.91 mA cm^{-2}, an open-circuit photovoltage of 710 mV and an efficiency of 5.88% with an incident photon-to-current conversion efficiency of 53%, while those for the NO_2-terminted dye (**Fe-29**) were slightly lower (see Table 1).

In 2021, Singh et al. reported five new 1,10-bis(diphenylphosphino)ferrocene-nickel(II) dithiolates (**Fe-30**, **Fe-31**, **Fe-32**, **Fe-33**, and **Fe-34**) bearing at least one cyano anchoring group and that differed by the aromatic substituent on the dithiolate chelating ligand, that is, phenyl, 2-cyanophenyl, 2-pyridyl, 3-pyridyl, and 2-thienyl ring (Figure 5) [115]. UV–Visible absorption spectra of all sensitizers recorded in dichloromethane showed strong bands at 280–350 nm due to intraligand charge transfer (ILCT), as well as weaker absorption in the 450–500 nm region attributed to *d–d* transition originating from the iron center. The electrochemistry of these photosensitizers was carried out in acetonitrile and showed a quasi-reversible oxidation event in the range between +0.445 and +0.715 V versus NHE. The reduction of these photosensitizers occurred in the range of −2.35 to −2.27 V versus NHE, again indicating possible electron injection into the TiO_2 surface. The photovoltaic properties of all the photosensitizers showed that those bearing a pyridine moiety, that is, **Fe-32** and **Fe-33**, performed the best, displaying an open-circuit photovoltage of −667 and −633 mV, photocurrents of 11.25 and 13.15 mA cm^{-2} as well as a fill factor of 0.63 and 0.61 resulting in overall efficiencies of 4.76% and 5.05%, respectively. It was hypothesized that the better performance was due to the presence of the pyridine group that could change the electronic properties of the photosensitizer. It is worth pointing out that pyridine can also serve as an anchoring group, and as such, these increased performances could originate from an improved photosensitizer loading [129–132].

Finally, in 2022, Chauhan et al. reported three ferrocenyl-2-pyridylimine complexes (**Fe-35**, **Fe-36**, and **Fe-37**, see Figure 5) that were composed of a bidentate pyridylimine unit capable of coordinating different d^{10}-metal centers such as Zn (II), Cd(II), and Hg(II) [116]. In this study, the complexes were employed in DSSC applications both as sole sensitizers or as a co-sensitizer in combination with the prototypical ruthenium N719 dye [133]. UV–Visible absorption showed maxima around 480 nm that extended up to 600 nm. **Fe-35**, whose pyridylimine unit is coordinated to Zn(II), showed the best performance in the photovoltaic study, not only as a sole sensitizer but also as a co-sensitizer. An open-circuit photovoltage of 684 mV, a photocurrent of 6.08 mA cm^{-2} with a fill factor of 0.67, and a conversion efficiency of 2.79% were determined. This superior performance compared to analog complexes (**Fe-36** and **Fe-37)** was attributed to better electron injection and reduced recombination, along with improved light harvesting ability of **Fe-35**, particularly in the 400–500 nm range. The **Fe-36**/N719 co-sensitizer also showed improved photovoltaic performance

28359399, 0, Downloaded from https://onlinelibrary.wiley.com/doi/10.1002/ece2.70001, Wiley Online Library on [09/03/2025]. See the Terms and Conditions (https://onlinelibrary.wiley.com/terms-and-conditions) on Wiley Online Library for rules of use; OA articles are governed by the applicable Creative Commons License

with an open-circuit photovoltage of 776 mV, a photocurrent of 11.25 mA cm^{-2} along with a fill factor of 0.65, and an efficiency of 5.71%.

3 | Conclusions and Perspectives

We have presented here a comprehensive overview of the iron photosensitizers that have been used in DSSCs applications. Genuinely, the photosensitizers only lead to moderate photocurrent and low overall efficiencies compared to the "champion" Ru(II) photosensitizers. In addition, there are currently no iron photosensitizers that have been used for the development of DSPECs. The pessimist might see the modest number of reports on iron photosensitizers as evidence that this field will not further develop, whereas the optimist will see this as the ground work of a much larger project that will unveil in the coming years. As such, we present avenues that we believe are worth exploring in order to tackle the challenges associated with developing iron photosensitizers for DSSCs and DSPECs applications.

- Tuning the driving force for electron transfer processes

Excited-state injection and regeneration of the photosensitizer represent a delicate interplay between ground- and excited-state redox potentials. If we consider the photoanode, the photosensitizer must have an excited-state potential sufficiently energetic to transfer an electron in the conduction band or acceptor states of the mesoporous material. On the other hand, the oxidized photosensitizer must have a Fe(III)/Fe(II) ground-state reduction potential (if the reaction is starting from Fe(II)) that is sufficiently positive to oxidize a redox mediator such as iodide (in the case of DSSC) or a catalyst (in the case of DSPEC). Almost quantitative excited-state charge injection has been reported [102], yet the overall photocurrents are still relatively small (Table 1). This often implies that back-electron transfer from the injected electron is fast or that the regeneration of the oxidized photosensitizer is slow [105]. Most of the iron photosensitizer presented herein have Fe(III)/Fe(II) potentials that are on average 300–500 mV more negative than the prototypical Ru(II) photosensitizers used in DSPECs. Thus, an avenue to explore would be to judiciously tune the ground-state potential to reach Fe(III)/Fe(II) potentials that are closer to the Ru(III)/Ru(II) couple, all while exhibiting an excited-state potential competent for injection into the photoanode. This would maximize the regeneration efficiency of the oxidized dye and also place the recombination from the injected electron further into the Marcus inverted region, assuming similar reorganization energies, thereby slowing down the recombination process. This could thus mitigate the ultrafast recombination between the injected electron and the oxidized photosensitizer. This challenging interplay between ground- and excited-state potentials is probably key to lead to more efficient architectures based on iron photosensitizers.

- Vectorial electron transfer

The notion of vectorial electron transfer has already been proposed in the literature and is also described in this review [134]. Vectorial electron transfer implies that, upon illumination, electron density is moved from the distal portion of the photosensitizer to the anchored side of the photosensitizer. In this simple picture, this would allow to maximize charge injection. Systems based on push–pull architectures have been presented [135–137], yet these systems often come at the cost of a lowered (more negative) oxidation potential, as the hole is transferred from the metal center to the distal portion of the photosensitizer via a redox gradient. Thus, the potential to drive useful transformation is decreased, and the recombination from injected electron occurs closer to the Marcus normal region for electron transfer. However, the benefit of that approach is to increase the distance between the injected electron and the hole, which could decrease the recombination rate constant.

Another approach toward vectorial electron transfer is to use heteroleptic complexes, where, according to Blakley and DeArmond, metal-to-ligand charge transfer is located on the ligand that is the most easily reduced [138]. Thus, by careful molecular engineering, the excited state could be fully localized on the ligand that is anchored on the metal oxide, thereby favoring excited-state charge injection. A testimony to that approach is evident in complexes **Fe-10** to **Fe-15** where the excited state is localized on the anchored ligand and that all show overall higher efficiencies compared to other complexes. The challenge here is the complexity to obtain heteroleptic complexes that often proceed in a one-pot statistical reaction with complicated purification steps.

Finally, it is worth emphasizing the recent report of $[Fe(phtmeimb)_2]^+$, a luminescent iron(III) photosensitizer pioneered by Wärnmark and coworkers, where phtmeimb is phenyl[tris(3-methyl-imidazolin-2-ylidene)]borate [139, 140]. This photosensitizer exhibits a ligand-to-metal charge transfer (LMCT) excited state, where electron density is transferred from the ligand to the metal. At first, this is not in line with vectorial electron transfer that would be useful for the development of photoanodes, but this photosensitizer could be used for photocathode materials, where electron transfer away from the surface is needed. This approach could also further benefit from the development of heteroleptic photosensitizers, which is as challenging as for Fe(II)-based MLCT photosensitizers.

- Type of targeted transformations

A complexity in research is to move passed the state of the art and develop research without being influenced by the mainstream reports. As such, even if water oxidation appears like an ultimate goal for DPSECs due to the high abundance of water, this reaction is still thermodynamically and kinetically complicated. As such, developing alternative reactions that can be carried out at metal oxide interfaces (photoanode and photocathodes) will be key to the further development of iron photosensitizers. Very recently, K. Schanze and coworkers reported a radical cation Diels–Alder reaction that was carried out at a dye-sensitized photoanode using a prototypical Ru(II) photosensitizer [141]. Similar photosensitizers were used by G. Leem and coworkers for the photoelectrosynthesis conversion of lignin to value-added aromatics [142]. F. Li and coworkers reported the bromide-mediated photoelectrochemical epoxidation of alkenes at $BiVO_4$ electrodes [143]. Thus, there are several reactions that could be carried out on photoelectrodes if

28359399, 0, Downloaded from https://onlinelibrary.wiley.com/doi/10.1002/ece2.70001, Wiley Online Library on [09/03/2025]. See the Terms and Conditions (https://onlinelibrary.wiley.com/terms-and-conditions) on Wiley Online Library for rules of use; OA articles are governed by the applicable Creative Commons License

judiciously designed iron photosensitizers were to be used. Taking $[Fe(phtmeimb)_2]^+$ as an example, recent reports have shown that this photosensitizer was competent for bimolecular catalysis in solution for hydrogen production as well as for halide oxidation in an organic solvent [144, 145]. This complex has also been used in photoredox catalysis [146–148], and as such, it has shown great promise for light-induced transformations. Thus, such transformations, and others, could thus represent an attractive target for functional photoelectrodes. However, one has to keep fundamental aspects in mind. As mentioned earlier, $[Fe(phtmeimb)_2]^+$ exhibits an LMCT excited state, and as such, high photocurrent on photoanode materials is not expected. They would be extremely useful on photocathode materials for CO_2 or H^+ reduction. However, the photocathode represents the Achilles' heel of DSPECs. A typical metal oxide for photocathodes is NiO, a material with a large concentration of lattice defects that lead to small charge-carrier lifetimes and electrical mobilities [149]. Although high surface loading of photosensitizers is commonly achieved on mesoporous anatase TiO_2 thin films (5–10 $\times$ 10^{-8} mol cm^{-2}), the surface coverage of NiO electrodes remains extremely low and reaches 5%–10% of surface coverages obtainable on TiO_2 and SnO_2. This already represents a challenge for Ru(II) photosensitizers with a molar absorption coefficient of ~15 000 $M^{-1}cm^{-1}$ around 450 nm [150] but will certainly be exacerbated using $[Fe(phtmeimb)_2]^+$ that exhibits a low molar absorption coefficient of ~3000 $M^{-1}cm^{-1}$ at 500 nm [139]. Thus, strategies to increase the molar absorption coefficient of these LMCT photosensitizers would also be beneficial for the future development of sensitized photocathodes.

Acknowledgments

L.T.-G. is a Chercheur Qualifié of the Fonds de la Recherche Scientifique—FNRS. All the authors gratefully acknowledge the UCLouvain for financial support. This publication benefited from the support of the Walloon Region as part of the financing of the FRFS-WEL-T strategic axis.

Conflicts of Interest

The authors declare no conflicts of interest.

Data Availability Statement

Data sharing not applicable to this article as no datasets were generated or analyzed during the current study.

References

1. T. P. Hughes, M. L. Barnes, D. R. Bellwood, et al., "Coral Reefs in the Anthropocene," *Nature* 546, no. 7656 (2017): 82–90.

2. L. Wang, X. Liu, L. Cao, et al., "Active Sites of Single-Atom Iron Catalyst for Electrochemical Hydrogen Evolution," *Journal of Physical Chemistry Letters* 11, no. 16 (2020): 6691–6696.

3. A. L. Hammond, "Solar Energy: The Largest Resource," *Science* 177, no. 4054 (1972): 1088–1090.

4. P. Sudhagar, N. Roy, R. Vedarajan, et al., "Hydrogen and CO_2 Reduction Reactions: Mechanisms and Catalysts," in *Photoelectrochemical Solar Fuel Production: From Basic Principles to Advanced Devices*, eds. S. Giménez and J. Bisquert (Cham: Springer International Publishing, 2016), 105–160.

5. N. S. Lewis and D. G. Nocera, "Powering the Planet: Chemical Challenges in Solar Energy Utilization," *PNAS* 103, no. 43 (2006): 15729–15735.

6. G. Ciamician, "The Photochemistry of the Future," *Science* 36, no. 926 (1912): 385–394.

7. H. Kaneko, T. Minegishi, M. Nakabayashi, et al., "A Novel Photocathode Material for Sunlight-Driven Overall Water Splitting: Solid Solution of ZnSe and $Cu(In,Ga)Se_2$," *Advances in Functional Materials* 26, no. 25 (2016): 4570–4577.

8. T. R. Cook, D. K. Dogutan, S. Y. Reece, Y. Surendranath, T. S. Teets, and D. G. Nocera, "Solar Energy Supply and Storage for the Legacy and Nonlegacy Worlds," *Chemistry Review* 110, no. 11 (2010): 6474–6502.

9. J. Su and L. Vayssieres, "A Place in the Sun for Artificial Photosynthesis?," *ACS Energy Letters* 1, no. 1 (2016): 121–135.

10. M. A. Green, E. D. Dunlop, M. Yoshita, et al., "Solar Cell Efficiency Tables (Version 63)," *Progress in Photovoltaics: Research and Applications* 32, no. 1 (2024): 3–13.

11. R. A. Marques Lameirinhas, J. P. N. Torres, and J. P. de Melo Cunha, "A Photovoltaic Technology Review: History, Fundamentals and Applications," *Energies* 15, no. 5 (2022): 1823.

12. A. Vlad, N. Singh, J. Rolland, S. Melinte, P. M. Ajayan, and J. F. Gohy, "Hybrid Supercapacitor-Battery Materials for Fast Electrochemical Charge Storage," *Scientific Reports* 4, no. 1 (2014): 4315.

13. A. Vlad, N. Singh, C. Galande, and P. M. Ajayan, "Design Considerations for Unconventional Electrochemical Energy Storage Architectures," *Advanced Energy Materials* 5, no. 19 (2015): 1402115.

14. B. Dunn, H. Kamath, and J.-M. Tarascon, "Electrical Energy Storage for the Grid: A Battery of Choices," *Science* 334, no. 6058 (2011): 928–935.

15. D. Larcher and J. M. Tarascon, "Towards Greener and More Sustainable Batteries for Electrical Energy Storage," *Nature Chemistry* 7, no. 1 (2015): 19–29.

16. S. Berardi, S. Drouet, L. Francas, et al., "Molecular Artificial Photosynthesis," *Chemical Society Reviews* 43, no. 22 (2014): 7501–7519.

17. C. Liu, B. C. Colón, M. Ziesack, P. A. Silver, and D. G. Nocera, "Water Splitting-Biosynthetic System With CO_2 Reduction Efficiencies Exceeding Photosynthesis," *Science* 352, no. 6290 (2016): 1210–1213.

18. D. Antón-García, E. Edwardes Moore, M. A. Bajada, et al., "Photoelectrochemical Hybrid Cell for Unbiased CO_2 Reduction Coupled to Alcohol Oxidation," *Nature Synthesis* 1, no. 1 (2022): 77–86.

19. S. Bhattacharjee, M. Rahaman, V. Andrei, et al., "Photoelectrochemical CO_2-to-Fuel Conversion With Simultaneous Plastic Reforming," *Nature Synthesis* 2, no. 2 (2023): 182–192.

20. N. Armaroli and V. Balzani, "The Future of Energy Supply: Challenges and Opportunities," *Angewandte Chemie International Edition* 46, no. 1–2 (2007): 52–66.

21. A. M. Abudayyeh, O. Schott, G. S. Hanan, and S. Brooker, "Copper Catalysts for Photo- and Electro-Catalytic Hydrogen Production," *Inorganic Chemistry Frontiers* 8, no. 4 (2021): 1015–1029.

22. A. Fujishima and K. Honda, "Electrochemical Photolysis of Water at a Semiconductor Electrode," *Nature* 238, no. 5358 (1972): 37–38.

23. C.-T. Dinh, A. Jain, F. P. G. de Arquer, et al., "Multi-Site Electrocatalysts for Hydrogen Evolution in Neutral Media by Destabilization of Water Molecules," *Nature Energy* 4, no. 2 (2018): 107–114.

24. I. Roger, M. A. Shipman, and M. D. Symes, "Earth-Abundant Catalysts for Electrochemical and Photoelectrochemical Water Splitting," *Nature Reviews Chemistry* 1 (2017): 0003.

25. M.-R. Gao, J.-X. Liang, Y.-R. Zheng, et al., "An Efficient Molybdenum Disulfide/Cobalt Diselenide Hybrid Catalyst for Electrochemical Hydrogen Generation," *Nature Communications* 6, no. 1 (2015): 5982.

28359399, 0, Downloaded from https://onlinelibrary.wiley.com/doi/10.1002/ece2.70001, Wiley Online Library on [09/03/2025]. See the Terms and Conditions (https://onlinelibrary.wiley.com/terms-and-conditions) on Wiley Online Library for rules of use; OA articles are governed by the applicable Creative Commons License

26. T. Takata, J. Jiang, Y. Sakata, et al., "Photocatalytic Water Splitting With a Quantum Efficiency of Almost Unity," *Nature* 581, no. 7809 (2020): 411–414.

27. T. Hisatomi, J. Kubota, and K. Domen, "Recent Advances in Semiconductors for Photocatalytic and Photoelectrochemical Water Splitting," *Chemical Society Reviews* 43, no. 22 (2014): 7520–7535.

28. Q. Wang, J. Warnan, S. Rodríguez-Jiménez, et al., "Molecularly Engineered Photocatalyst Sheet for Scalable Solar Formate Production From Carbon Dioxide and Water," *Nature Energy* 5, no. 9 (2020): 703–710.

29. Y. Ham, T. Hisatomi, Y. Goto, et al., "Flux-Mediated Doping of $SrTiO_3$ Photocatalysts for Efficient Overall Water Splitting," *Journal of Materials Chemistry* 4, no. 8 (2016): 3027–3033.

30. Y. Goto, T. Hisatomi, Q. Wang, et al., "A Particulate Photocatalyst Water-Splitting Panel for Large-Scale Solar Hydrogen Generation," *Joule* 2, no. 3 (2018): 509–520.

31. K. Maeda and K. Domen, "Photocatalytic Water Splitting: Recent Progress and Future Challenges," *Journal of Physical Chemistry Letters* 1, no. 18 (2010): 2655–2661.

32. H. Lyu, T. Hisatomi, Y. Goto, et al., "An Al-Doped $SrTiO_3$ Photocatalyst Maintaining Sunlight-Driven Overall Water Splitting Activity for Over 1000 H of Constant Illumination," *Chemical Science* 10, no. 11 (2019): 3196–3201.

33. H. Gerischer, "On the Role of Electrons and Holes in Surface Reactions on Semiconductors," *Surface Science* 13, no. 1 (1969): 265–278.

34. H. Gerischer, *Physical Chemistry: An Advanced Treatise*, eds. H. Eyring, et al., (New York: Academic Press, 1970), 487–489.

35. A. J. Bard, "Photoelectrochemistry and Solar Energy: Progress, Promise and Problems," *Journal of Electroanalytical Chemistry and Interfacial Electrochemistry* 168, no. 1 (1984): 5–20.

36. B. O'Regan and M. Grätzel, "A Low-Cost, High-Efficiency Solar Cell Based on Dye-Sensitized Colloidal TiO_2 Films," *Nature* 353, no. 6346 (1991): 737–740.

37. H. Gerischer and H. Tributsch, "Elektrochemische Untersuchungen zur spektralen Sensibilisierung von ZnO-Einkristallen," *Berichte der Bunsen-Gesellschaft für Physikalische Chemie* 72, no. 3 (1968): 437–445.

38. H. Tributsch and H. Gerischer, "The Use of Semiconductor Electrodes in the Study of Photochemical Reactions," *Berichte der Bunsen-Gesellschaft* 73, no. 8–9 (1969): 850–854.

39. H. Tributsch and H. Gerischer, "Elektrochemische Untersuchungen über den Mechanismus der Sensibilisierung und übersensibilisierung an ZnO-Einkristallen," *Berichte der Bunsen-Gesellschaft* 73, no. 3 (1969): 251–260.

40. S. Anderson, E. C. Constable, M. P. Dare-Edwards, et al., "Chemical Modification of a Titanium (IV) Oxide Electrode to Give Stable Dye Sensitisation Without a Supersensitiser," *Nature* 280, no. 5723 (1979): 571–573.

41. A. Kirsch-De Mesmaeker, M. Rochus-Dewitt, and J. Nasielski, "Photoelectrochemical Transients Induced by Pulsed Laser Illumination of the Tin Dioxide/Tris(2,2'-Bipyridine)Ruthenium(II) Solution Interface at Different pH's," *Journal of Physical Chemistry* 90, no. 25 (1986): 6657–6662.

42. A. Kirsch-De Mesmaeker, J. Nasielski, and R. Willem, "Photoelectrochemistry of Ru(bpy)32+ in Basic Medium at SnO_2 and Metal Electrodes," *Bulletin des Societes Chimiques Belges* 91, no. 9 (1982): 731–742.

43. H. Taube, H. Myers, and R. L. Rich, "Observations on the Mechanism of Electron Transfer in Solution," *Journal of the American Chemical Society* 75, no. 16 (1953): 4118–4119.

44. R. A. Marcus, "On the Theory of Oxidation-Reduction Reactions Involving Electron Transfer. I," *Journal of Chemical Physics* 24, no. 5 (1956): 966–978.

45. P. R. Smith and J. W. Richardson, "Electron Density Shifts During Chemical Bond Formation," *Journal of Physical Chemistry* 69, no. 10 (1965): 3346–3357.

46. H. Gerischer, "Electrochemical Techniques for the Study of Photosensetizers," *Photochemistry and Photobiology* 16, no. 4 (1972): 243–260.

47. A. Heller, B. Miller, and F. A. Thiel, "11.5% Solar Conversion Efficiency in the Photocathodically Protected p-InP/V^{3+}-V^{2+}-HCI/C Semiconductor Liquid Junction Cell," *Applied Physics Letters* 38, no. 4 (1981): 282–284.

48. A. Heller, "Conversion of Sunlight Into Electrical Power and Photoassisted Electrolysis of Water in Photoelectrochemical Cells," *Accounts of Chemical Research* 14, no. 5 (1981): 154–162.

49. H. Gerischer, "Electrochemical Photo and Solar Cells Principles and Some Experiments," *Journal of Electroanalytical Chemistry and Interfacial Electrochemistry* 58, no. 1 (1975): 263–274.

50. G. Hodes, J. Manassen, and D. Cahen, "Photoelectrochemical Energy Conversion and Storage Using Polycrystalline Chalcogenide Electrodes," *Nature* 261, no. 5559 (1976): 403–404.

51. N. Alonso, M. Beley, P. Chartier, and V. Ern, "Dye Sensitization of Ceramic Semiconducting Electrodes for Photoelectrochemical Conversion," *Revue de Physique Appliquee* 16, no. 1 (1981): 5–10.

52. M. Matsumura, Y. Nomura, and H. Tsubomura, "Dye-Sensitization on the Photocurrent at Zinc Oxide Electrode in Aqueous Electrolyte Solution," *BCSJ* 50, no. 10 (2006): 2533–2537.

53. E. Marchini, S. Caramori, and S. Carli, "Metal Complexes for Dye-Sensitized Photoelectrochemical Cells (DSPECs)," *Mol* 29, no. 2 (2024): 293.

54. K. L. Materna, R. H. Crabtree, and G. W. Brudvig, "Anchoring Groups for Photocatalytic Water Oxidation on Metal Oxide Surfaces," *Chemical Society Reviews* 46, no. 20 (2017): 6099–6110.

55. L. Zhang and J. M. Cole, "Anchoring Groups for Dye-Sensitized Solar Cells," *ACS Applied Materials and Interfaces* 7, no. 6 (2015): 3427–3455.

56. R. Bangle, R. N. Sampaio, L. Troian-Gautier, and G. J. Meyer, "Surface Grafting of Ru(II) Diazonium-Based Sensitizers on Metal Oxides Enhances Alkaline Stability for Solar Energy Conversion," *ACS Applied Materials and Interfaces* 10, no. 3 (2018): 3121–3132.

57. A. B. Muñoz-García, I. Benesperi, G. Boschloo, et al., "Dye-Sensitized Solar Cells Strike Back," *Chemical Society Reviews* 50, no. 22 (2021): 12450–12550.

58. B. O'Regan, L. Xiaoe, and T. Ghaddar, "Dye Adsorption, Desorption, and Distribution in Mesoporous TiO_2 Films, and Its Effects on Recombination Losses in Dye Sensitized Solar Cells," *Energy & Environmental Science* 5, no. 5 (2012): 7203–7215.

59. Z. Yang, S. Gao, T. Li, F.-Q. Liu, Y. Ren, and T. Xu, "Enhanced Electron Extraction From Template-Free 3D Nanoparticulate Transparent Conducting Oxide (TCO) Electrodes for Dye-Sensitized Solar Cells," *ACS Applied Materials and Interfaces* 4, no. 8 (2012): 4419–4427.

60. B. Tan, E. Toman, Y. Li, and Y. Wu, "Zinc Stannate (Zn_2SnO_4) Dye-Sensitized Solar Cells," *Journal of the American Chemical Society* 129, no. 14 (2007): 4162–4163.

61. C. A. Bignozzi, S. Caramori, V. Cristino, R. Argazzi, L. Meda, and A. Tacca, "Nanostructured Photoelectrodes Based on WO_3: Applications to Photooxidation of Aqueous Electrolytes," *Chemical Society Reviews* 42, no. 6 (2013): 2228–2246.

62. S. N. Karthick, K. V. Hemalatha, S. K. Balasingam, F. Manik Clinton, S. Akshaya, and H.-J. Kim, "Dye-Sensitized Solar Cells: History, Components, Configuration, and Working Principle," in *Interfacial Engineering in Functional Materials for Dye-Sensitized Solar Cells*, (2019), 1–16, https://doi.org/10.1002/9781119557401.ch1.

63. K. Y. Chen, P. A. Schauer, B. O. Patrick, and C. P. Berlinguette, "Correlating Cobalt Redox Couples to Photovoltage in the Dye-

28359399, 0, Downloaded from https://onlinelibrary.wiley.com/doi/10.1002/ece2.70001, Wiley Online Library on [09/03/2025]. See the Terms and Conditions (https://onlinelibrary.wiley.com/terms-and-conditions) on Wiley Online Library for rules of use; OA articles are governed by the applicable Creative Commons License

Sensitized Solar Cell," *Dalton Transactions* 47, no. 34 (2018): 11942–11952.

64. G. Oskam, B. V. Bergeron, G. J. Meyer, and P. C. Searson, "Pseudohalogens for Dye-Sensitized TiO_2 Photoelectrochemical Cells," *Journal of Physical Chemistry B* 105, no. 29 (2001): 6867–6873.

65. M. Wang, N. Chamberland, L. Breau, et al., "An Organic Redox Electrolyte to Rival Triiodide/Iodide in Dye-Sensitized Solar Cells," *Nature Chemistry* 2, no. 5 (2010): 385–389.

66. C. A. Kelly, F. Farzad, D. W. Thompson, J. M. Stipkala, and G. J. Meyer, "Cation-Controlled Interfacial Charge Injection in Sensitized Nanocrystalline TiO_2," *Langmuir* 15, no. 20 (1999): 7047–7054.

67. T. A. Heimer, E. J. Heilweil, C. A. Bignozzi, and G. J. Meyer, "Electron Injection, Recombination, and Halide Oxidation Dynamics at Dye-Sensitized Metal Oxide Interfaces," *Journal of Materials Chemistry A* 104, no. 18 (2000): 4256–4262.

68. D. F. Watson and G. J. Meyer, "Electron Injection at Dye-Sensitized Semiconductor Electrodes," *Annual Review of Physical Chemistry* 56, no. 1 (2005): 119–156.

69. L. Troian-Gautier, W. B. Swords, and G. J. Meyer, "Iodide Photoredox and Bond Formation Chemistry," *Accounts of Chemical Research* 52, no. 1 (2019): 170–179.

70. K.-R. Wee, B. D. Sherman, M. K. Brennaman, et al., "An Aqueous, Organic Dye Derivatized SnO_2/TiO_2 Core/Shell Photoanode," *Journal of Materials Chemistry A* 4, no. 8 (2016): 2969–2975.

71. L. Alibabaei, M. K. Brennaman, M. R. Norris, et al., "Solar Water Splitting in a Molecular Photoelectrochemical Cell," *PNAS* 110, no. 50 (2013): 20008–20013.

72. L. Troian-Gautier, R. N. Sampaio, E. J. Piechota, M. D. Brady, and G. J. Meyer, "Barriers for Interfacial Back-Electron Transfer: A Comparison Between TiO_2 and SnO_2/TiO_2 Core/Shell Structures," *Journal of Chemical Physics* 150, no. 4 (2018).

73. L. Xiao, J. A. Spies, C. J. Sheehan, et al., "Electron Transfer Dynamics at Dye-Sensitized SnO_2/TiO_2 Core/Shell Electrodes in Aqueous/Nonaqueous Electrolyte Mixtures," *Journal of the American Chemical Society* 146, no. 26 (2024): 18117–18127.

74. N. S. McCool, J. R. Swierk, C. T. Nemes, C. A. Schmuttenmaer, and T. E. Mallouk, "Dynamics of Electron Injection in SnO_2/TiO_2 Core/Shell Electrodes for Water-Splitting Dye-Sensitized Photoelectrochemical Cells," *Journal of Physical Chemistry Letters* 7, no. 15 (2016): 2930–2934.

75. M. D. Brady, R. N. Sampaio, D. Wang, T. J. Meyer, and G. J. Meyer, "Dye-Sensitized Hydrobromic Acid Splitting for Hydrogen Solar Fuel Production," *Journal of the American Chemical Society* 139, no. 44 (2017): 15612–15615.

76. M. V. Sheridan, Y. Wang, D. Wang, et al., "Light-Driven Water Splitting Mediated by Photogenerated Bromine," *Angewandte Chemie International Edition* 57, no. 13 (2018): 3449–3453.

77. L. Troian-Gautier, M. D. Turlington, S. A. M. Wehlin, et al., "Halide Photoredox Chemistry," *Chemistry Review* 119, no. 7 (2019): 4628–4683.

78. Y. Wang, X. Meng, K. Jeong, et al., "Investigation of a Lignin-Based Deep Eutectic Solvent Using P-Hydroxybenzoic Acid for Efficient Woody Biomass Conversion," *ACS Sustainable Chemistry & Engineering* 8, no. 33 (2020): 12542–12553.

79. S. Li, Z.-J. Li, H. Yu, et al., "Solar-Driven Lignin Oxidation via Hydrogen Atom Transfer With a Dye-Sensitized TiO_2 Photoanode," *ACS Energy Letters* 5, no. 3 (2020): 777–784.

80. J. A. Treadway, J. A. Moss, and T. J. Meyer, "Visible Region Photooxidation on TiO_2 With a Chromophore – Catalyst Molecular Assembly," *Inorganic Chemistry* 38, no. 20 (1999): 4386–4387.

81. W. J. Youngblood, S.-H. A. Lee, Y. Kobayashi, et al., "Photoassisted Overall Water Splitting in a Visible Light-Absorbing Dye-Sensitized Photoelectrochemical Cell," *Journal of the American Chemical Society* 131, no. 3 (2009): 926–927.

82. A. Harriman, I. J. Pickering, J. M. Thomas, and P. A. Christensen, "Metal Oxides as Heterogeneous Catalysts for Oxygen Evolution under Photochemical Conditions," *Journal of the Chemical Society, Faraday Transactions* 84, no. 8 (1988): 2795–2806.

83. L. Li, L. Duan, F. Wen, et al., "Visible Light Driven Hydrogen Production From a Photo-Active Cathode Based on a Molecular Catalyst and Organic Dye-Sensitized P-Type Nanostructured NiO," *Chemical Communications* 48, no. 7 (2012): 988–990.

84. B. Shan, S. Vanka, T.-T. Li, et al., "Binary Molecular-Semiconductor P–N Junctions for Photoelectrocatalytic CO_2 Reduction," *Nature Energy* 4, no. 4 (2019): 290–299.

85. D. Wang, R. N. Sampaio, L. Troian-Gautier, et al., "Molecular Photoelectrode for Water Oxidation Inspired by Photosystem II," *Journal of the American Chemical Society* 141, no. 19 (2019): 7926–7933.

86. F. Niu, D. Wang, L. J. Williams, et al., "A Semiconductor-Mediator-Catalyst Artificial Photosynthetic System for Photoelectrochemical Water Oxidation," *Chemistry - A European Journal* 28, no. 10 (2022): e202102630.

87. Q. Loague, N. D. Keller, A. V. Müller, et al., "Impact of Molecular Orientation on Lateral and Interfacial Electron Transfer at Oxide Interfaces," *ACS Applied Materials and Interfaces* 15, no. 28 (2023): 34249–34262.

88. R. E. Bangle, M. J. Mortelliti, L. Troian-Gautier, J. L. Dempsey, and G. J. Meyer, "Tunneling and Thermally Activated Electron Transfer in Dye-Sensitized $SnO_2|TiO_2$ Core|Shell Nanostructures," *Journal of Materials Chemistry C: Materials for Optical and Electronic Devices* 124, no. 45 (2020): 25148–25159.

89. E. M. James, M. T. Bennett, and G. J. Meyer, "Electroabsorption as a Probe of Electrons Injected Into Nanocrystalline SnO_2/TiO_2 Core/Shell Thin Films," *Journal of Materials Chemistry C: Materials for Optical and Electronic Devices* 127, no. 12 (2023): 5904–5910.

90. W. A. Smith, "Photoelectrochemical Cell Design, Efficiency, Definitions, Standards, and Protocols," in *Photoelectrochemical Solar Fuel Production: From Basic Principles to Advanced Devices*, eds. S. Giménez and J. Bisquert (Cham: Springer International Publishing, 2016), 163–197.

91. A. Hagfeldt, G. Boschloo, L. Sun, L. Kloo, and H. Pettersson, "Dye-Sensitized Solar Cells," *Chemistry Review* 110, no. 11 (2010): 6595–6663.

92. M. Pastore, S. Caramori, and P. C. Gros, "Iron-Sensitized Solar Cells (FeSSCs)," *Accounts of Chemical Research* 57, no. 4 (2024): 439–449.

93. C. Costentin, S. Drouet, M. Robert, and J.-M. Savéant, "Turnover Numbers, Turnover Frequencies, and Overpotential in Molecular Catalysis of Electrochemical Reactions. Cyclic Voltammetry and Preparative-Scale Electrolysis," *Journal of the American Chemical Society* 134, no. 27 (2012): 11235–11242.

94. S. Kozuch and J. M. L. Martin, "'Turning Over' Definitions in Catalytic Cycles," *ACS Catalysis* 2, no. 12 (2012): 2787–2794.

95. T. Bessho, E. C. Constable, M. Graetzel, et al., "An Element of Surprise—Efficient Copper-Functionalized Dye-Sensitized Solar Cells," *Chemical Communications*, no. 32 (2008): 3717–3719.

96. D. Sayah and T. H. Ghaddar, "Copper-Based Aqueous Dye-Sensitized Solar Cell: Seeking a Sustainable and Long-Term Stable Device," *ACS Sustainable Chemistry & Engineering* 12, no. 16 (2024): 6424–6432.

97. F. Fagnani, A. Colombo, C. Dragonetti, and D. Roberto, "Recent Investigations on the Use of Copper Complexes as Molecular Materials for Dye-Sensitized Solar Cells," *Mol* 29, no. 1 (2024): 6.

98. Z. Singh, P. R. Donnarumma, and M. B. Majewski, "Molecular Copper(I)–Copper(II) Photosensitizer–Catalyst Photoelectrode for Water Oxidation," *Inorganic Chemistry* 59, no. 18 (2020): 12994–12999.

28359399, 0, Downloaded from https://onlinelibrary.wiley.com/doi/10.1002/ece2.70001, Wiley Online Library on [09/03/2025]. See the Terms and Conditions (https://onlinelibrary.wiley.com/terms-and-conditions) on Wiley Online Library for rules of use; OA articles are governed by the applicable Creative Commons License

99. S. Ferrere, "New Photosensitizers Based Upon $[Fe(L)_2(CN)_2]$ and $[Fe(L)_3]$ (L = Substituted 2,2'-Bipyridine): Yields for the Photosensitization of TiO_2 and Effects on the Band Selectivity," *Chemistry of Materials* 12, no. 4 (2000): 1083–1089.

100. S. Ferrere and B. A. Gregg, "Photosensitization of TiO_2 by [FeII (2,2'-Bipyridine-4,4'-Dicarboxylic acid)$_2$(CN)$_2$]: Band Selective Electron Injection From Ultra-Short-Lived Excited States," *Journal of the American Chemical Society* 120, no. 4 (1998): 843–844.

101. T. Duchanois, T. Etienne, C. Cebrián, et al., "An Iron-Based Photosensitizer With Extended Excited-State Lifetime: Photophysical and Photovoltaic Properties," *European Journal of Inorganic Chemistry* 2015, no. 14 (2015): 2469–2477.

102. T. C. B. Harlang, Y. Liu, O. Gordivska, et al., "Iron Sensitizer Converts Light to Electrons With 92% Yield," *Nature Chemistry* 7, no. 11 (2015): 883–889.

103. R. N. Sampaio, L. Troian-Gautier, and G. J. Meyer, "A Charge-Separated State That Lives for Almost a Second at a Conductive Metal Oxide Interface," *Angewandte Chemie International Edition* 57, no. 47 (2018): 15390–15394.

104. A. Reddy-Marri, E. Marchini, V. D. Cabanes, et al., "Panchromatic Light Harvesting and Record Power Conversion Efficiency for Carboxylic/Cyanoacrylic Fe(ii) NHC Co-Sensitized FeSSCs," *Chemical Science* 14, no. 16 (2023): 4288–4301.

105. L. Lindh, O. Gordivska, S. Persson, et al., "Dye-Sensitized Solar Cells Based on Fe N-Heterocyclic Carbene Photosensitizers With Improved Rod-Like Push-Pull Functionality," *Chemical Science* 12, no. 48 (2021): 16035–16053.

106. T. Duchanois, L. Liu, M. Pastore, et al., "NHC-Based Iron Sensitizers for DSSCs," *Inorga* 6, no. 2 (2018): 63.

107. M. Pastore, T. Duchanois, L. Liu, et al., "Interfacial Charge Separation and Photovoltaic Efficiency in Fe(ii)–Carbene Sensitized Solar Cells," *Physical Chemistry Chemical Physics* 18, no. 40 (2016): 28069–28081.

108. A. Reddy Marri, E. Marchini, V. D. Cabanes, et al., "Record Power Conversion Efficiencies for Iron(ii)-NHC-Sensitized DSSCs From Rational Molecular Engineering and Electrolyte Optimization," *Journal of Materials Chemistry A* 9, no. 6 (2021): 3540–3554.

109. A. R. Marri, E. Marchini, V. D. Cabanes, et al., "A Series of Iron (II)-NHC Sensitizers With Remarkable Power Conversion Efficiency in Photoelectrochemical Cells," *Chemistry - A European Journal* 27, no. 65 (2021): 16260–16269.

110. A. M. El-Zohry, J. Cong, M. Karlsson, L. Kloo, and B. Zietz, "Ferrocene as a Rapid Charge Regenerator in Dye-Sensitized Solar Cells," *Dyes and Pigments* 132 (2016): 360–368.

111. A. Ghosh, S. Mishra, S. Giri, S. M. Mobin, A. Bera, and S. Chatterjee, "Electrolyte-Free Dye-Sensitized Solar Cell With High Open Circuit Voltage Using a Bifunctional Ferrocene-Based Cyanovinyl Molecule as Dye and Redox Couple," *Organometallics* 37, no. 13 (2018): 1999–2002.

112. A. H. Anizaim, D. A. Zainuri, M. F. Zaini, I. A. Razak, H. Bakhtiar, and S. Arshad, "Comparative Analyses of New Donor-π-Acceptor Ferrocenyl-Chalcones Containing Fluoro and Methoxy-Fluoro Acceptor Units as Synthesized Dyes for Organic Solar Cell Material," *PLoS One* 15, no. 11 (2020): e0241113.

113. A. H. Anizaim, M. F. Zaini, I. A. Razak, and S. Arshad, "Insight Into the Impact of the Substituent Modification on the Photovoltaic Performance of Ferrocenyl Chalcones Based DSSCs," *Journal of Solid State Chemistry* 304 (2021): 122551.

114. A. Singh, G. Kociok-Köhn, R. Chauhan, M. Muddassir, S. W. Gosavi, and A. Kumar, "Ferrocene Appended Asymmetric Sensitizers With Azine Spacers With Phenolic/Nitro Anchors for Dye-Sensitized Solar Cells," *Journal of Molecular Structure* 1249 (2022): 131630.

115. A. Singh, A. Dutta, D. Srivastava, et al., "Effect of Different Aromatic Groups on Photovoltaic Performance of 1,1′-Bis (Diphenylphosphino)ferrocene Functionalized Ni (II) Dithiolates as Sensitizers in Dye Sensitized Solar Cells," *Applied Organometallic Chemistry* 35, no. 11 (2021): e6402.

116. C. Gautam, A. Singh, S. W. Gosavi, et al., "Ferrocenyl-2-Pyridylimine Derived D10-Configuration Complexes as Prospective Co-Sensitizers in Dye Sensitized Solar Cells," *Applied Organometallic Chemistry* 36, no. 4 (2022): e6608.

117. I. Jinchu, C. O. Sreekala, and K. S. Sreelatha, "Lawsone Metal Complex as an Effective Sensitizer for Dye Sensitized Solar Cells," *Materials Today Proceedings* 33 (2020): 1356–1360.

118. H. Setyawati, M. S. Hadi, H. Darmokoesoemo, I. K. Murwani, A. J. Permana, and F. Rochman, "Modification of Methyl Orange Dye as a Light Harvester on Solar Cell," *IOP Conference Series: Earth and Environmental Science* 456, no. 1 (2020): 012010.

119. F. Glaser, A. Aydogan, B. Elias, and L. Troian-Gautier, "The Great Strides of Iron Photosensitizers for Contemporary Organic Photoredox Catalysis: On Our Way to the Holy Grail?," *Coordination Chemistry Reviews* 500 (2024): 215522.

120. C. Creutz, M. Chou, T. L. Netzel, M. Okumura, and N. Sutin, "Lifetimes, Spectra, and Quenching of the Excited States of Polypyridine Complexes of Iron(II), Ruthenium(II), and Osmium(II)," *Journal of the American Chemical Society* 102, no. 4 (1980): 1309–1319.

121. J. K. McCusker, K. N. Walda, R. C. Dunn, J. D. Simon, D. Magde, and D. N. Hendrickson, "Sub-Picosecond .DELTA.S = 2 Intersystem Crossing in Low-Spin Ferrous Complexes," *Journal of the American Chemical Society* 114, no. 17 (1992): 6919–6920.

122. A. L. Smeigh, M. Creelman, R. A. Mathies, and J. K. McCusker, "Femtosecond Time-Resolved Optical and Raman Spectroscopy of Photoinduced Spin Crossover: Temporal Resolution of Low-to-High Spin Optical Switching," *Journal of the American Chemical Society* 130, no. 43 (2008): 14105–14107.

123. E. A. Juban, A. L. Smeigh, J. E. Monat, and J. K. McCusker, "Ultrafast Dynamics of Ligand-Field Excited States," *Coordination Chemistry Reviews* 250, no. 13–14 (2006): 1783–1791.

124. J. K. McCusker, "Electronic Structure in the Transition Metal Block and Its Implications for Light Harvesting," *Science* 363, no. 6426 (2019): 484–488.

125. C. Förster and K. Heinze, "Bimolecular Reactivity of 3D Metal-Centered Excited States (Cr, Mn, Fe, Co)," *Chemical Physics Reviews* 3, no. 4 (2022).

126. Y. Liu, T. Harlang, S. E. Canton, et al., "Towards Longer-Lived Metal-to-Ligand Charge Transfer States of Iron(ii) Complexes: An N-Heterocyclic Carbene Approach," *Chemical Communications* 49, no. 57 (2013): 6412–6414.

127. L. Lindh, T. Pascher, S. Persson, et al., "Multifaceted Deactivation Dynamics of Fe(II) N-Heterocyclic Carbene Photosensitizers," *Journal of Materials Chemistry A* 127, no. 48 (2023): 10210–10222.

128. S. Fery-Forgues and B. Delavaux-Nicot, "Ferrocene and Ferrocenyl Derivatives in Luminescent Systems," *Journal of Photochemistry and Photobiology A: Chemistry* 132, no. 3 (2000): 137–159.

129. X. Yan, K. Sakai, and H. Ozawa, "Highly Efficient and Stable Molecular-Based TiO_2 Photoanodes for Photoelectrochemical Water Splitting Achieved by Pyridyl Anchoring Technique," *ACS Catalysis* 13, no. 20 (2023): 13456–13465.

130. N. Shibayama, H. Ozawa, M. Abe, Y. Ooyama, and H. Arakawa, "A New Cosensitization Method Using the Lewis Acid Sites of a TiO_2 Photoelectrode for Dye-Sensitized Solar Cells," *Chemical Communications* 50, no. 48 (2014): 6398–6401.

131. N. Shibayama, H. Ozawa, Y. Ooyama, and H. Arakawa, "Highly Efficient Cosensitized Plastic-Substrate Dye-Sensitized Solar Cells With Black Dye and Pyridine-Anchor Organic Dye," *BCSJ* 88, no. 2 (2014): 366–374.

28359399, 0, Downloaded from https://onlinelibrary.wiley.com/doi/10.1002/ece2.70001, Wiley Online Library on [09/03/2025]. See the Terms and Conditions (https://onlinelibrary.wiley.com/terms-and-conditions) on Wiley Online Library for rules of use; OA articles are governed by the applicable Creative Commons License

132. K. Takijiri, K. Morita, T. Nakazono, K. Sakai, and H. Ozawa, "Highly Stable Chemisorption of Dyes With Pyridyl Anchors Over TiO_2: Application in Dye-Sensitized Photoelectrochemical Water Reduction in Aqueous Media," *Chemical Communications* 53, no. 21 (2017): 3042–3045.

133. C. Klein, M. K. Nazeeruddin, D. Di Censo, P. Liska, and M. Grätzel, "Amphiphilic Ruthenium Sensitizers and Their Applications in Dye-Sensitized Solar Cells," *Inorganic Chemistry* 43, no. 14 (2004): 4216–4226.

134. D.-H. Roh, J.-H. Park, H.-G. Han, et al., "Molecular Design Strategy for Realizing Vectorial Electron Transfer in Photoelectrodes," *Chem* 8, no. 4 (2022): 1121–1136.

135. C. Bourguignon, A. Moinel, A. Huet, et al., "Photoelectrochemical Hydrogen Production by a Cobalt Tetrapyridyl Catalyst Using Push–Pull Dye-Sensitized NiO Photocathodes," *Advanced Energy and Sustainability Research* 4, no. 12 (2023): 2300095.

136. J. Wang, V. Gadenne, L. Patrone, and J.-M. Raimundo, "Self-Assembled Monolayers of Push–Pull Chromophores as Active Layers and Their Applications," *Mol* 29, no. 3 (2024): 559.

137. Z. Parsa, S. S. Naghavi, and N. Safari, "Designing Push–Pull Porphyrins for Efficient Dye-Sensitized Solar Cells," *Journal of Materials Chemistry A* 122, no. 27 (2018): 5870–5877.

138. R. L. Blakley and M. K. DeArmond, "Unique Spectroscopic Properties of Mixed-Ligand Complexes With 2,2'-Dipyridylamine: A Dual Luminescence From a Ruthenium(II) Complex," *Journal of the American Chemical Society* 109, no. 16 (1987): 4895–4901.

139. K. S. Kjær, N. Kaul, O. Prakash, et al., "Luminescence and Reactivity of a Charge-Transfer Excited Iron Complex With Nanosecond Lifetime," *Science* 363, no. 6424 (2019): 249–253.

140. O. Prakash, L. Lindh, N. Kaul, et al., "Photophysical Integrity of the Iron(III) Scorpionate Framework in Iron(III)–NHC Complexes With Long-Lived 2LMCT Excited States," *Inorganic Chemistry* 61, no. 44 (2022): 17515–17526.

141. M. D. Turlington, S. Ahmed, and K. S. Schanze, "Radical Cation Diels–Alder Reaction by Photocatalysis at a Dye Sensitized Photoanode," *ACS Catalysis* 14, no. 16 (2024): 12512–12517.

142. S. Li, S. Park, B. D. Sherman, C. G. Yoo, and G. Leem, "Photoelectrochemical Approaches for the Conversion of Lignin at Room Temperature," *Chemical Communications* 59, no. 4 (2023): 401–413.

143. X. Liu, Z. Chen, S. Xu, et al., "Bromide-Mediated Photoelectrochemical Epoxidation of Alkenes Using Water as an Oxygen Source With Conversion Efficiency and Selectivity up to 100," *Journal of the American Chemical Society* 144, no. 43 (2022): 19770–19777.

144. J. Schwarz, A. Ilic, C. Johnson, R. Lomoth, and K. Wärnmark, "High Turnover Photocatalytic Hydrogen Formation With an Fe(III) N-Heterocyclic Carbene Photosensitiser," *Chemical Communications* 58, no. 35 (2022): 5351–5354.

145. S. De Kreijger, A. Ripak, B. Elias, and L. Troian-Gautier, "Investigation of the Excited-State Electron Transfer and Cage Escape Yields Between Halides and a Fe(III) Photosensitizer," *Journal of the American Chemical Society* 146, no. 15 (2024): 10286–10292.

146. A. Aydogan, R. E. Bangle, A. Cadranel, et al., "Accessing Photoredox Transformations With an Iron(III) Photosensitizer and Green Light," *Journal of the American Chemical Society* 143, no. 38 (2021): 15661–15673.

147. A. Aydogan, R. E. Bangle, S. De Kreijger, et al., "Mechanistic Investigation of a Visible Light Mediated Dehalogenation/Cyclisation Reaction Using Iron(iii), Iridium(iii) and Ruthenium(ii) Photosensitizers," *Catalysis Science and Technology* 11, no. 24 (2021): 8037–8051.

148. A. Ilic, B. R. Strücker, C. E. Johnson, S. Hainz, R. Lomoth, and K. Wärnmark, "Aminomethylations of Electron-Deficient Compounds—Bringing Iron Photoredox Catalysis Into Play," *Chemical Science* 15, no. 30 (2024): 12077–12085.

149. C. J. Flynn, S. M. McCullough, L. Li, C. L. Donley, Y. Kanai, and J. F. Cahoon, "Passivation of Nickel Vacancy Defects in Nickel Oxide Solar Cells by Targeted Atomic Deposition of Boron," *Journal of Materials Chemistry C: Materials for Optical and Electronic Devices* 120, no. 30 (2016): 16568–16576.

150. F. Glaser, S. De Kreijger, K. Achilleos, et al., "A Compendium of Methodically Determined Ground- and Excited-State Properties of Homoleptic Ruthenium(II) and Osmium(II) Photosensitizers," *ChemPhotoChem* (2024): e202400134.

28359399, 0, Downloaded from https://onlinelibrary.wiley.com/doi/10.1002/ece2.70001, Wiley Online Library on [09/03/2025]. See the Terms and Conditions (https://onlinelibrary.wiley.com/terms-and-conditions) on Wiley Online Library for rules of use; OA articles are governed by the applicable Creative Commons License